Materials Science & Engineering A 881 (2023) 145373

Contents lists available at ScienceDirect

Materials Science & Engineering A

journal homepage: www.elsevier.com/locate/msea

Application of a nanoindentation-based approach for parameter identification to a crystal plasticity model for bcc metals

Francisco-José Gallardo-Basile [a,*], Franz Roters [a], Robin M. Jentner [a], James P. Best [a], Christoph Kirchlechner [b], Kinshuk Srivastava [c], Sebastian Scholl [c], Martin Diehl [d,e]

[a] Max–Planck-Institut für Eisenforschung, Max–Planck-Straße 1, 40237 Düsseldorf, Germany
[b] Institute for Applied Materials (IAM), Karlsruhe Intitute of Technology (KIT), Kaiserstraße 12, 76131 Karlsruhe, Germany
[c] AG der Dillinger Hüttenwerke, Werkstraße 1, 66763 Dillingen/Saar, Germany
[d] Department of Materials Engineering, KU Leuven, Kasteelpark Arenberg 44, 3001 Leuven, Belgium
[e] Department of Computer Science, KU Leuven, Celestijnenlaan 200A, 3001 Leuven, Belgium

ARTICLE INFO

Keywords:
Nanoindentation
Micropillar compression
Inverse modeling
Crystal plasticity
Bcc metals

ABSTRACT

The application of an inverse method for determining the parameters of a crystal plasticity constitutive law of a body-centered-cubic (BCC) single phase material is presented. Nanoindentation is used as the primary experimental input. An objective function, based on the deviation between the experimentally measured imprint and the simulated one, is minimized by a differential evolution algorithm to obtain the best fitting crystal plasticity parameters. To aid the identification procedure additional experimental data is used: the upper bounds and the ratios of the critical resolved shear stresses of the three slip plane families in BCC are estimated from micropillar compression experiments and used as a constraint in the optimization. The effect of the imposed constraints and the chosen strategy for mapping experimental to simulated displacements is presented and discussed. The validation of the method is done in the macroscopic regime by comparing an experimental tensile test with a simulated one using the obtained crystal plasticity parameters. Accurate results are achieved from two different indents. Therefore, the method is a promising path for determining crystal plasticity parameters in the case where a direct fitting from a macroscopic stress–strain curve is not possible, i.e. in the case of multi-phase materials.

1. Introduction

Crystal plasticity (CP) modeling is an established approach for predicting the mechanical response of metals and alloys [1,2]. A critical point when employing a CP model is the identification of its constitutive parameters. The large amount of parameters and the strong non-linear coupling between them renders this a tedious task. Without correct parameters, CP models cannot be used for predicting and understanding the mechanical behavior of metallic materials.

Parameters for a CP constitutive model describe the single crystal behavior, but still can be obtained from polycrystalline macroscopic stress–strain curves coming from either unidirectional tension or compression tests [3–6]. Herrera-Solaz et al. [6] determined the single crystal properties of a magnesium alloy from experimental stress–strain curves along different directions. The calculated set of CP parameters was able to accurately predict the stress–strain behavior of the polycrystal. Sedighiani et al. [7] were able to identify reliable parameters that were sensitive to strain-rate and temperature through a series of tensile test experiments. In all the above studies, the polycrystal behavior was obtained by means of a CP simulation of a representative volume element (RVE) of the microstructure. This RVE is usually obtained from sufficiently large and detailed electron backscatter diffraction (EBSD) scans. The measured 2D orientation maps are used to construct either 2D or 3D RVEs that are aiming to capture the relevant properties of the microstructure. One of the most important properties in CP modeling is texture, hence reproducing the experimental orientation distribution function (ODF) into the RVE is a necessary step to correctly match the simulated and the real mechanical behavior [8]. Other statistical quantities like grain morphology, grain size, grain shape, grain orientation spread, etc., may also be included [9,10]. After the RVE creation, the parameters of a constitutive law are obtained by fitting a simulated macroscopic stress–strain curve to the experimental one. The simulated curve is based on the RVE as the microstructure and a constitutive law with parameters to describe the mechanical behavior.

The information obtained from tensile tests might not be sufficient to obtain a physically correct set of parameters. For face-centered-cubic (FCC) metals, where slip occurs mainly along ⟨1 1 0⟩ directions

* Corresponding author.
E-mail address: f.gallardo@mpie.de (F.-J. Gallardo-Basile).

https://doi.org/10.1016/j.msea.2023.145373
Received 11 October 2022; Received in revised form 18 April 2023; Accepted 23 June 2023
Available online 30 June 2023

on {1 1 1} planes, the identification is possible if the constitutive model itself is not over-parameterized. In hexagonal-close-packed (HCP) metals, plastic deformation can be realized due to slip or twinning on various slip and twin systems. Due to the hexagonal symmetry and the vastly different critical resolved shear stresses (CRSS) for the different deformation modes, different deformation systems are activated when loading a textured material in different loading directions [11]. This can be exploited to unambiguously identify CP parameters for HCP materials. Body-centered-cubic (BCC) metals, in contrast, have many potential slip systems with a similar CRSS. Commonly observed slip systems in BCC comprise of ⟨1 1 1⟩ directions on {1 1 0}, {1 1 2}, and {1 2 3} planes [12]. This is due to the non-close packed nature of the BCC lattice together with the fact that its plasticity is governed by glide of screw dislocations, which are not confined to a well-defined glide plane [13]. Therefore, the unique parametrization of CP models for BCC metals is more challenging than for FCC and HCP metals.

Alternative methods have been developed when macroscopic tensile tests cannot be used to obtain CP parameters. This is for example the case for multi-phase materials, where the problem regarding the uniqueness of the solution considerably aggravates when using macroscopic quantities. When seeking to model each individual phase of the material, many combinations of the stress–strain curves of the multiple phases reproduce a given bulk stress–strain curve, i.e. the correct solution cannot be obtained. In such cases, a more direct way for determining CP parameters are micro- or nano-mechanical tests of individual grains. Bertin et al. [14] and Du et al. [15] used ferritic bi- and single crystals, respectively, to obtain CP parameters from micro tensile tests. They, however, did not show a comparison to a macroscopic tensile test of a polycrystal made of the same material. Another mechanical test at a micro- or nano-scale is pillar compression, which was used by Ghassemi-Armaki et al. [16] to determine CP parameters. The micropillars contained a single block of martensite and were claimed to be in the bulk regime (where results are expected to be size-independent). However, extracting reliable material parameters with this method has several shortcomings: material properties can be altered by the pillar preparation in the focused ion beam microscope, a misalignment of the set-up leads to a complex stress state and not considering the impact of the friction and the elastic–plastic buckling on the force–displacement data is another source of error [17]. Although the yield stress can artifact-free be extracted under certain conditions, a direct and meaningful interpretation of the strain hardening in micropillar experiments is not possible [17].

Another class of tests for the determination of CP parameters that allows to probe individual grains but does not require the labor intensive fabrication of micro tensile samples or pillars is instrumented nanoindentation. It consists on indenting a hard tip into the surface of the material while measuring force and displacement. The two main inverse analysis techniques that can be employed to extract mechanical properties of materials from instrumented indentation experimental data are: the representative stress–strain method [18–20] and the iterative finite element analysis. The iterative method has been used extensively in the past for rather simple isotropic power laws which describe the plastic behavior of metal materials with a small amount of parameters to be fitted [21–25]. Zambaldi et al. [26] were the first to combine nanoindentation, EBSD orientation mapping, and atomic force microscopy (AFM) topographic measurements to derive single phase constitutive parameters of HCP alpha titanium for a CP model. They used both the surface imprint and the load–displacement for the optimization procedure. Tasan et al. [27] applied the same inverse technique as Zambaldi et al. [26] for BCC ferrite in a dual phase material, while the martensite parameters were obtained through fitting to macroscopic stress–strain curves. Chakraborty and Eisenlohr [28] demonstrated the reliability of the inverse indentation analysis using single crystal nanoindentation for an FCC metal with a similar procedure using both the surface imprint and the load–displacement curve. Shahmardani et al. [29] identified the parameters of a non-local CP model for a BCC material using the inverse modeling with nanoindentation. However, in Zambaldi et al. [26], Tasan et al. [27], Chakraborty and Eisenlohr [28], Shahmardani et al. [29], validation of the results was not done on a macroscopic level. Engels et al. [30] applied an inverse method using nanoindentation for tempered lath martensite. The validation of the identified parameters was done by comparing numerical and experimental stress–strain curves of a macroscopic tensile test. For one of the alloys, the results depended strongly on the indent used for the optimization. Whether the source of error comes from the difficulty of describing the lath martensite microstructure, lath martensite plasticity, or the inverse method itself remained unclear.

Here, the application of an inverse method for determining the CP parameters of a ferritic material is presented. The main experimental input is nanoindentation, as described above. A differential evolution method is employed to minimize an objective function based on the difference between the experimentally observed imprint and the simulated one to provide the best fitting CP parameters. As a novelty, the use of additional data from micropillar compression experiments to assist the parameters identification is implemented. In a macroscopic domain, the CP parameters are validated by contrasting an experimental tensile test with a simulated one. The goal of the paper is to show the validity of this method to obtain CP parameters for a BCC material and to discuss which aspects play a dominant role in order to get accurate results.

This study is structured as follows: In Section 2, the experimental aspects are described. The CP modeling framework is described in Section 3. The details of the optimization method are explained in Section 4. In Section 5, results are shown. Discussion about key aspects is presented in Section 6 and finally, a summary and outlook are given.

2. Material and methods

The material used is described in Section 2.1. In what follows, the experimental methods required for the inverse method are outlined. The micropillar compressions (see Section 2.2) were done at room temperature to obtain the CRSS for each slip plane family, which will be used directly as constraints for the parameters optimization (see Section 4.1). The nanoindentation experiments (see Section 2.3) are done in order to analyze the post-mortem imprint with atomic force microscopy (see Section 2.6). This imprint will be compared to a simulated one to evaluate the objective function (see Section 4.4). Lastly, in order to characterize the macroscopic behavior of the material, EBSD scans (see Section 2.3) and tensile tests (see Section 2.5) are carried out. EBSD scans are done to characterize the microstructure of the material and build the RVE (see Section 3.2). The tensile tests provide the macroscopic mechanical behavior of the material, which will be part of the macroscopic validation presented in Section 5.

2.1. Material

A high-strength low-alloy steel with a chemical composition of Fe-0.05C-0.32Si-1.45Mn (wt%) was heat-treated first for 72 h at 1150°C and then at 750°C for another 5 h to produce large polygonal ferrite grains without substructure.

2.2. Micropillar compression

Micro compression tests at room temperature were carried out using a *Zeiss Auriga* dual-beam scanning electron microscope (SEM) on OPS polished specimens. Pillars with a top diameter of 5 μm and a targeted aspect ratio of 2 were milled with a 30 keV Ga^+ beam in three steps: the first outer ring was cut with 2 nA, 600 pA were used for the middle ring, and a last polishing step was done with 240 pA. The tapper angle was kept below 2° for every pillar. All micropillars were tested *in situ* inside a *Zeiss Gemini500* SEM equipped with a

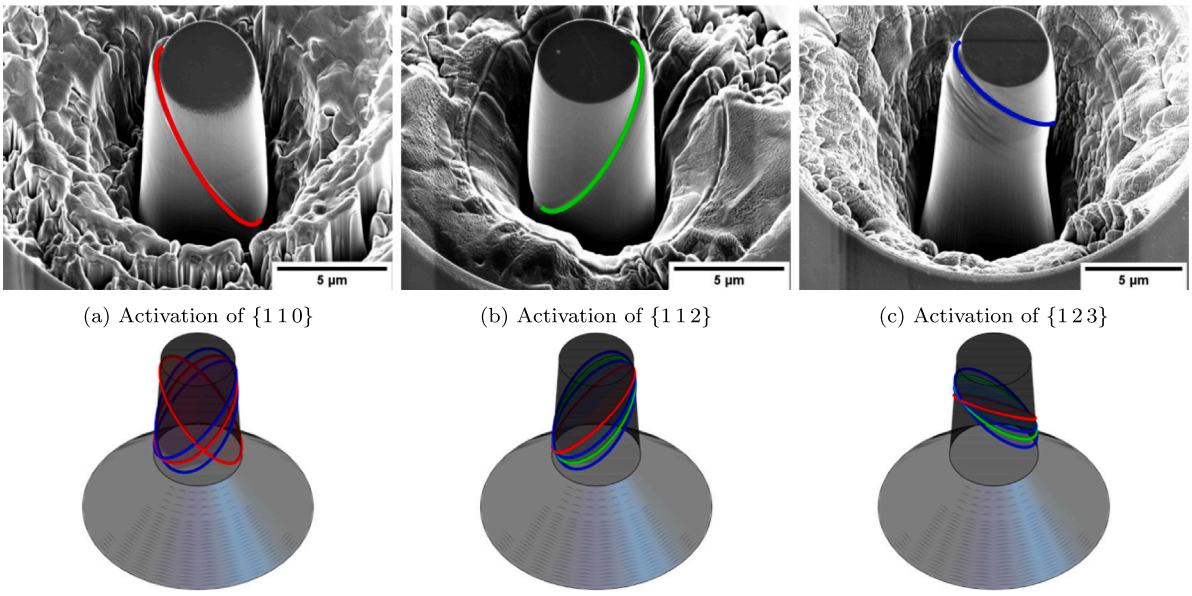

(a) Activation of {1 1 0} (b) Activation of {1 1 2} (c) Activation of {1 2 3}

(d) The four slip planes with the highest Schmid factors for (a). (e) The four slip planes with the highest Schmid factors for (b) (f) The four slip planes with the highest Schmid factors for (c)

Fig. 1. Top row shows scanning electron microscopy images of three representative tested micropillars of the {1 1 0}→(red), {1 1 2}→(green) and {1 2 3}→(blue) slip plane families. Bottom row shows slip planes with the four highest Schmid factors. (For interpretation of the references to color in this figure legend, the reader is referred to the web version of this article.)

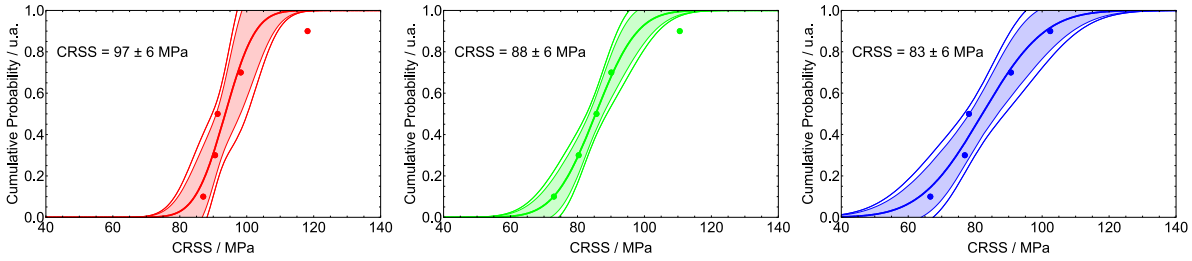

(a) CRSS for {1 1 0} (b) CRSS for {1 1 2} (c) CRSS for {1 2 3}

Fig. 2. Cumulative probability of the CRSS for each slip plane family. The average value and the 90% and 95% confidence bands are shown.

Bruker Hysitron PI88 system. The average value of the top and bottom pillar diameter as well as the pillar height was used to calculate the engineering stress and strain values. Finally, the CRSS of each pillar was calculated by multiplying the stress at an engineering strain of 2 % and the Schmid factor m of the activated slip system. For each pillar, given the measured crystallographic orientation, the CRSS was calculated for all 48 considered slip systems. Subsequently, a prediction is made of the slip planes with the highest Schmid factors. SEM is used to obtain images of the micropillars and carry out a correlative *post mortem* analysis to determine the activated slip plane similar to Tian et al. [31]. This correlative analysis is shown in Fig. 1 where the slip plane families {1 1 0}, {1 1 2}, and {1 2 3} are colored in red, green, and blue respectively. In Figs. 1(a)–1(c), SEM images are shown where the activated slip plane is overlaid in the image. In Figs. 1(d)–1(f), the four slip planes with the highest Schmid factors are displayed.

A total number of 15 micropillars were tested. The orientation of the pillars was chosen based on the predicted slip plane activated in order to have 5 pillars per slip plane family. The results are shown in Fig. 2, where a cumulative distribution is used to calculate an average value and its standard deviation for the CRSS for each slip plane family. The average values are 97 MPa, 88 MPa, and 83 MPa for the {1 1 0}, {1 1 2}, and {1 2 3} slip plane families respectively. For all three values, the standard error of the mean was determined as ±6 MPa.

The orientations of the 15 micropillars are plotted in Fig. 3 into an inverse pole figure (IPF) with respect to the micropillar compression axis. Each point is colored according to the experimentally identified activated slip plane family. The background of the IPF is colored by the predicted slip plane family based on the Schmid factor. All the pillars followed Schmid's law. The activation of all slip plane families and the satisfaction of Schmid's law is in agreement with literature. Tian et al. [31] demonstrated that ferritic pillars in a dual phase steel showed the activation of all three possible slip plane families all owning a ⟨1 1 1⟩ Burgers vector at comparable CRSS. They also showed that the majority of pillars followed Schmid's law and non-Schmid effects do not play a significant role in slip activation at room temperature. This is expected since non-Schmid effects in *Fe* are negligible at room temperature [32,33].

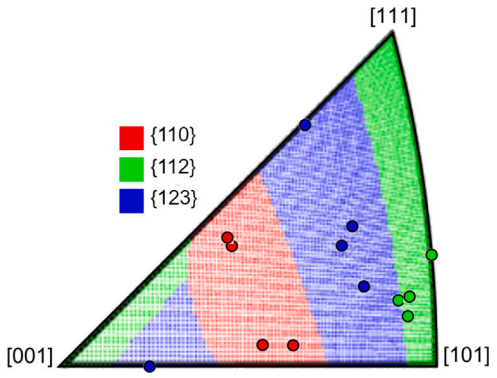

Fig. 3. Inverse pole figure triangle normal to the micropillar compression axis showing where the {1 1 0},{1 1 2}, or {1 2 3} slip plane families have the highest Schmid factor. The tested micropillar orientations are plotted with the color according to experimentally identified activated slip plane family. (For interpretation of the references to color in this figure legend, the reader is referred to the web version of this article.)

2.3. Nanoindentation

Nanoindentation tests on a grid were performed using a *Hysitron TriboIndenter 950*. The diamond indenter had a sphero-conical shape with a nominal cone angle of 90° and a tip radius of 1 µm. The tip area function was calibrated against fused silica. All experiments were conducted in load-controlled conditions with a maximum force of 2.5 mN and a loading–holding–unloading time of 10 s–5 s–10 s. The indentations were arranged in a regular grid with a spacing of 20 µm. A total of 2700 indentations were distributed in sections parallel to ND, TD, and RD. EBSD scans were done after the indentation to correlate each indent to a crystallographic orientation. Hardness and reduced Young's modulus were evaluated according to the Oliver–Pharr method [34].

As an example, the output data from a single indentation is shown in Fig. 4. Before point A, the indenter approaches the surface, which can be seen in the displacement in Fig. 4(c) before t = 0. Since no contact is yet established, the load is 0 in Figs. 4(a) and 4(b). From the contact point A on-wards, the sample is loaded and elastic and plastic deformation of the sample occurs. At point B, the holding phase starts. It is worth mentioning that some plasticity is still occurring during this phase with constant load, since some displacement is present from B to C. At point C, the unloading phase starts until point D, where the indenter and the sample are no longer in contact.

2.4. Electron backscatter diffraction

First, the heat-treated samples were ground with SiC-paper up to 2000 grit. Afterwards, they were polished with a suspension made of 30 nm aluminum particles. Finally, the EBSD measurement was done in a *Zeiss Auriga* dual-beam scanning electron microscope equipped with an EDAX system. A scan area of 400 µm × 400 µm was measured perpendicular to all three surfaces (TD × ND, RD × ND, and RD × TD) with an acceleration voltage of 20 kV and a step size of 0.40 µm. The data acquisition was done with the *TSL OIM* 8 software package. A small amount of austenite (≈0.3 %) was measured in the sample but neglected during the analysis.

2.5. Tensile test

The macroscopic behavior of the material was assessed by carrying out tensile tests. For this, electrical discharge machining was used for cutting the tensile test samples into a rectangular shaped cross section of 8 mm × 3 mm (TD × ND) and a gauge length of 30 mm (RD). A *ZwickRoell Z100* universal testing machine was used to perform all tensile tests in RD at room temperature and at a strain rate of $10^{-3}\,s^{-1}$. Since all three tests gave similar results with the biggest deviation being 8 MPa for a given strain, a single data-set of the macroscopic experimental tensile tests is used for comparison with the simulation results.

2.6. Atomic force microscopy

Selected indents were characterized topographically with a *Dimension 3100* instrument. The measurements of the height at the surface of the material were carried out in tapping mode with a tetrahedral silicon tip of 1 µm. Three zones are clearly distinguishable; the sink-in, the pile-up, and the zone not affected by the indent. Different patterns in the pile-up area are formed depending on the orientation of the crystal being indented. The data acquisition and subsequent calculations were done with the software *Gwyddion* [35]. An example of how the data was processed is shown in Fig. 5. The resolution of the images that were taken was 512 px × 512 px with a physical size of 5 µm × 5 µm. Thus each pixel represents a square of dimensions 9.8 nm × 9.8 nm.

From Fig. 5(a) it is visible that the height is not homogeneous outside the region affected by the indentation. The left side is colored in red tones (negative height) compared to the right side with blue tones (positive height). This indicates that the surface is tilted with respect to the AFM measurement direction. Therefore, it is also tilted with respect to the indentation performed, assuming that the indentation and the AFM measurement are vertically aligned. The tilted surface is approximated by a first degree polynomial in 2D, i.e. a plane (see Fig. 5(b)) based on the non-affected area. This tilt of the surface is later on introduced into the simulation modeling. The subtraction of this plane from the original raw image outputs the result in Fig. 5(c). For the comparison with simulation required in later stages, two pieces of information need to be obtained from the AFM image in Fig. 5(c): the center of the indentation, that is, the first contact point between the indenter and the surface, and the absolute height. The pixel with the lowest height after surface correction is assumed to be the center. The maximum depth is taken from the load–displacement curve and assigned to the indentation center (see Fig. 5(a)).

3. Modeling framework

DAMASK [36] is used as the crystal plasticity modeling framework. A phenomenological power law implemented therein is used as the constitutive law for the simulations. This CP model is an adoption of the phenomenological description of Hutchinson [37] (for details see [1]). Assuming that dislocation slip is the only deformation process, the plastic velocity gradient, $\mathbf{L}_p$, reads

$$\mathbf{L}_p = \sum_{\alpha=1}^{N} \dot{\gamma}^{\alpha} \mathbf{m}^{\alpha} \otimes \mathbf{n}^{\alpha} \tag{1}$$

where vectors $\mathbf{m}^{\alpha}$ and $\mathbf{n}^{\alpha}$ are, respectively, unit vectors describing the slip direction and the normal to the slip plane of the slip system α and N is the number of (active) slip systems; $\dot{\gamma}^{\alpha}$ is the shear rate on that same system. The kinetic law on a slip system follows

$$\dot{\gamma}^{\alpha} = \dot{\gamma}_0 \left| \frac{\tau^{\alpha}}{\xi^{\alpha}} \right|^{n} \operatorname{sgn}(\tau^{\alpha}) \tag{2}$$

with $\dot{\gamma}_0$ as reference shear rate, $\tau^{\alpha} = \mathbf{S} \cdot (\mathbf{m}^{\alpha} \otimes \mathbf{n}^{\alpha})$, and n the stress exponent. The microstructure is parameterized in terms of a slip resistance ξ^{α} on the twelve $\langle 1\,1\,1 \rangle \{1\,1\,0\}$ slip systems, the twelve $\langle 1\,1\,1 \rangle \{1\,1\,2\}$ slip systems, and the twentyfour $\langle 1\,1\,1 \rangle \{1\,2\,3\}$ slip systems, indexed by $\alpha = 1, \ldots, 48$. These resistances evolve asymptotically from ξ_0 towards ξ_{∞} with shear γ^{α} according to the relationship

$$\dot{\xi}^{\alpha} = h_0 \times q_{\alpha\alpha'} \times \sum_{\alpha'=1}^{N_s} \left| \dot{\gamma}^{\alpha'} \right| \left| 1 - \frac{\xi^{\alpha'}}{\xi_{\infty}^{\alpha'}} \right|^{a} \operatorname{sgn}\left(1 - \frac{\xi^{\alpha'}}{\xi_{\infty}^{\alpha'}} \right) \tag{3}$$

where h_0, a and ξ_{∞} are hardening parameters and $q_{\alpha\alpha'}$ are the components of the slip–slip interaction matrix, which describes the interaction between the different slip systems.

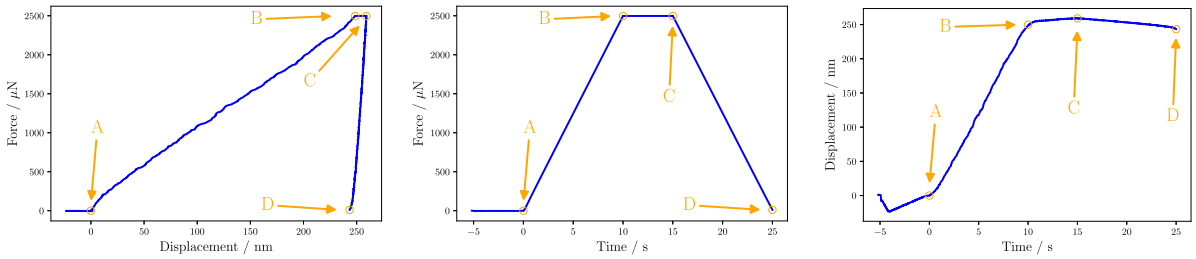

(a) Load–displacement curve (b) Load–time curve (c) Displacement–time curve

Fig. 4. Output data from a single indentation. Points A, B, and C correspond to the beginning of the load, hold, and unload phase, respectively. Point D is the end of the unload phase.

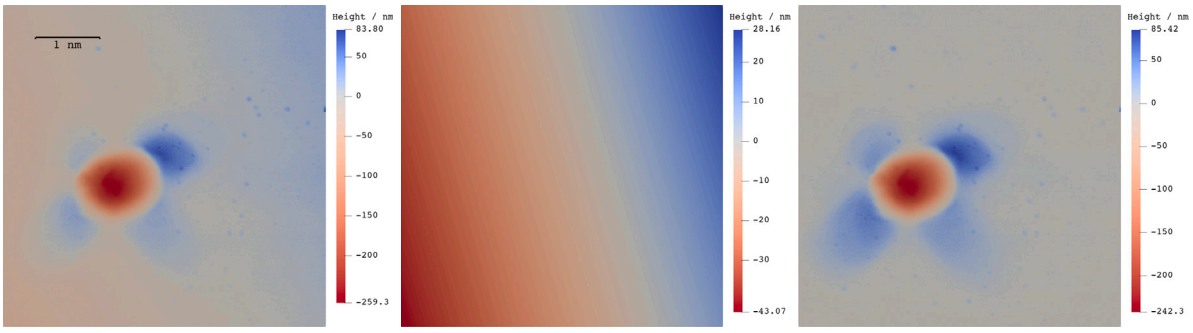

(a) Raw image (b) Background plane (c) Corrected image

Fig. 5. The raw AFM image is shown in (a). The background plane is shown in (b). The results of subtracting (b) from (a) is shown in (c) and referred to as 'corrected' image. (For interpretation of the references to color in this figure legend, the reader is referred to the web version of this article.)

3.1. Microscopic modeling – nanoindentation

In order to simulate nanoindentation experiments, DAMASK is coupled to MSC.Marc (commercial finite element software) by using the material subroutine *hypela2* to simulate the material behavior. Three different bodies are used as shown in Fig. 6(a): the sample made of the modeled material as a pillar in yellow, the indenter, and a sample holder. The two last bodies that are colored in blue correspond to geometric bodies (also referred as rigid bodies) and were modeled using non-uniform rational basis splines (NURBS). Note that the height of the cylindrical part of the indenter is irrelevant since this part is not in contact with the sample at any time during the simulation. The body in yellow is a meshed body (usually referred as a deformable body), which consists of finite elements. The sample holder is fixed and glued to the bottom of the sample, which suppresses all relative motions between bodies through boundary conditions applied to all the displacement and rotational degrees of freedom of the nodes in contact. The tilt described in Section 2.6 is incorporated into the model which is shown in Fig. 6 and referred to as the angle ϑ.

The sample is meshed using the STABIX toolbox by Mercier et al. [38]. Three different, coarse base meshes consisting of hexahedral elements (see Fig. 7) are first created. Only one quarter of each mesh is displayed, as the other 3 parts are symmetrically equal. The difference between the meshes, apart from the number of elements, is the aspect ratio of the elements. Mesh A (Fig. 7(a)) is made of very distorted elements. In the top part on the surface, distorted elements with their longest dimension in the XY-plane plane can be seen. In the bottom part, distorted elements with longest direction in Z direction can be seen. Mesh B (Fig. 7(b)) is made of less distorted elements. Mesh C (Fig. 7(c)) is made of the least distorted elements. All the meshes are denser close to the center to resolve the high deformation where the contact happens and the pile-ups used for the parameter identification occur.

Finer meshes with more elements are created through a direct refinement of these three meshes. The number of elements, the refinements used, and the maximum and minimum edge lengths are listed in Table 1. The mesh refinements are realized by dividing the element dimension in each direction by 2, 3, or 4, hence dividing each hexahedron into 8, 27, or 64 identical smaller hexahedra respectively.

For modeling friction, the force-based Coulomb friction model is used. It reads:

$$\mathbf{f}_t = -\mu f_n \cdot \mathbf{t} \tag{4}$$

where $\mathbf{f}_t$ is the tangential (friction) force, f_n is the normal force, μ is the friction coefficient and $\mathbf{t}$ is the tangential vector in the direction of the relative velocity. Since the discontinuity at $f_n = 0$ may easily cause numerical difficulties, a bi-linear model is used to approximate the step function.

An iterative penetration checking procedure is used for the determination of when contact occurs and the calculation of the normal vector. A full Newton–Raphson algorithm is used for the iterative procedures. Regarding the matrix solver for the calculation of the stiffness matrix, a symmetric solution is assumed for faster execution. A mixed direct iterative procedure is used as a symmetric matrix solver. The Multifrontal Sparse Solver is used to obtain a solution in the initial iteration of an increment while simultaneously generating the Cholesky pre-conditioner. The convergence criterion was based on minimizing both the relative residual forces and the relative displacements with an individual tolerance of 0.01 each. For more details about how MSC.Marc deals with contact and friction, see the manual [39].

3.2. Macroscopic modeling – tensile test

For the validation of the CP parameters at the macroscopic level, a simulated tensile test will be compared to an experimental one. The simulated polycrystal behavior is obtained by means of a CP simulation of a RVE of the microstructure. A spectral method using Fast Fourier

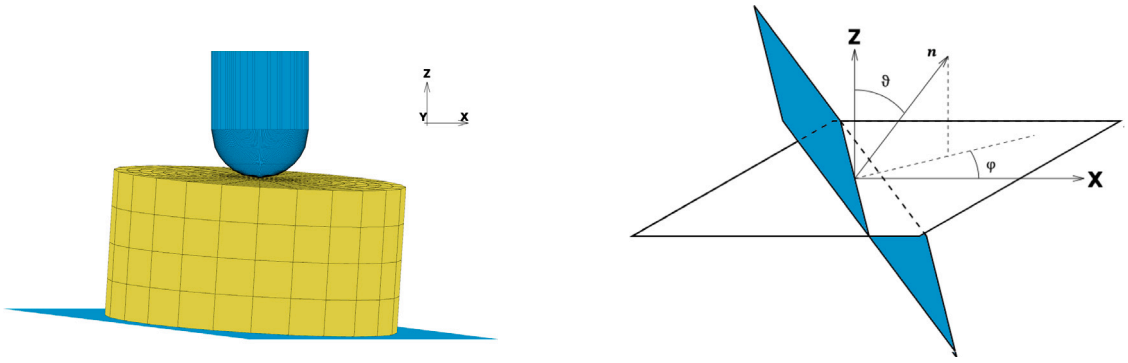

(a) Nanoindentation model (b) Tilt (ϑ) of the plane.

Fig. 6. The FEM nanoindentation modeling set-up is displayed in (a). Geometric bodies are colored in blue while the meshed body is colored in yellow. The rotation of the plane (sample holder) is better illustrated in (b) by the angles ϑ and φ. (For interpretation of the references to color in this figure legend, the reader is referred to the web version of this article.)

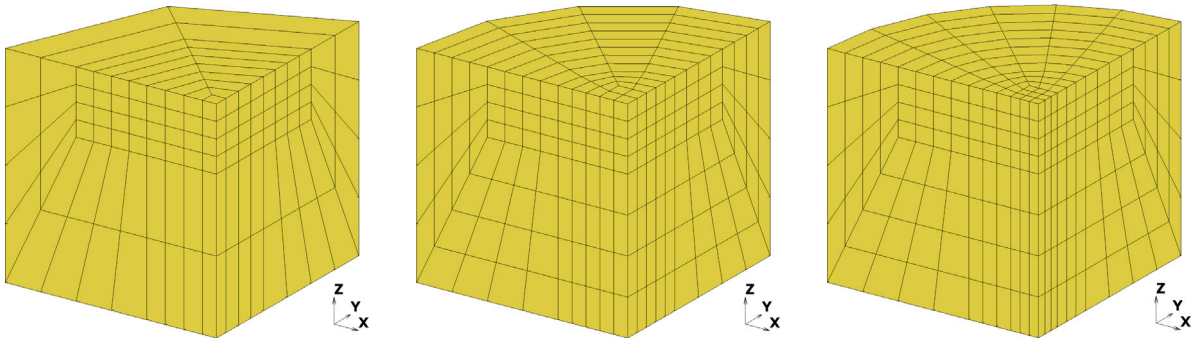

(a) Mesh A - 424 elements (b) Mesh B - 1280 elements (c) Mesh C - 2016 elements

Fig. 7. Different base meshes used in this investigation. Only one quarter is shown.

Table 1
Meshes obtained from the refinement of the base meshes A, B, and C.

Base mesh	A				B				C			
Refinement	1	2	3	4	1	2	3	4	1	2	3	4
Number of elements	424	3392	11 448	27 136	1280	10 240	34 560	81 920	2016	16 128	54 432	129 024
Minimum edge length/nm	198	99	66	50	143	72	48	36	132	66	44	33
Maximum edge length/nm	2296	1148	765	574	1171	585	390	293	783	392	261	196

Transforms (FFT) is used for iteratively solving the stress equilibrium problem [40,41]. Accordingly, a periodic RVE of the microstructure is build. To this end, EBSD scans were done perpendicular to the three planes TD × ND, RD × ND, and RD × TD. The grain size was measured using the linear intercept method. The results for the scans on the three surfaces (TD × ND, RD × ND, and RD × TD) were: 9.1 µm, 7.2 µm, and 13.5 µm for horizontal lines and 7.4 µm, 6.0 µm, and 11.0 µm for vertical lines, respectively. Based on these calculations, and the fact that there was no preferential orientation for the major axis of the grains, equiaxed grains were assumed for building the RVE. This feature as well as the grain size distribution were reproduced into the RVE by means of DREAM.3D [42]. The ODF from experimental results was calculated using MTEX [43] (Fig. 8(a)) using the combined data of all EBSD scans (RD, TD, and ND). A random sampling method was used for matching the texture of the RVE to the experimental one (Fig. 8(b)). Selecting a set of discrete orientations for accurate texture reconstruction was also done with the method proposed by Eisenlohr and Roters [44]. No significant changes were observed compared to a random sampling approach which was sufficient. This is due to the number of grains in the RVE being very high (2 644) and the texture being not very strong (the texture index is 1.2). Fig. 8(c) displays the difference between the experimental and the calculated pole figures for the RVE, showing minimum discrepancy.

4. Inverse modeling method for a CP model of a BCC material

The aim of an inverse modeling is to adjust the model parameters to reproduce a given result or target. Here, the output from the nanoindentation experiments, more specifically the imprint after the indentation, is used as a reference and the constitutive parameters of the CP model introduced in Section 3 are adjusted.

In order to have a reliable set of target data representative for the bulk material, only results from indents that are unaffected by grain boundaries are used. While it is trivial to measure the distance between grain boundaries and indents in the measurement plane, subsurface grain boundaries are more difficult to detect. To circumvent labor-intensive post-mortem serial sectioning to measure the distance to subsurface grain boundaries, here the indents are selected based on the quality of the results. More precisely, the imprints and hardness values of different indents into similarly oriented grains are compared and those indents that show a significantly different behavior are discarded.

Once the experimental input is selected, nanoindentation into grains of the same orientation is simulated. The difference in the height profile between the simulated and the experimental imprint on each of the N nodes is taken as the objective function λ:

$$\lambda = \frac{1}{N_{\text{active}}} \sum_{n=1}^{N_{\text{active}}} \left| u_n^{\text{sim}} - u_n^{\text{exp}} \right|, \text{n being nodes with } u_n^{\text{exp}} > 0 \tag{5}$$

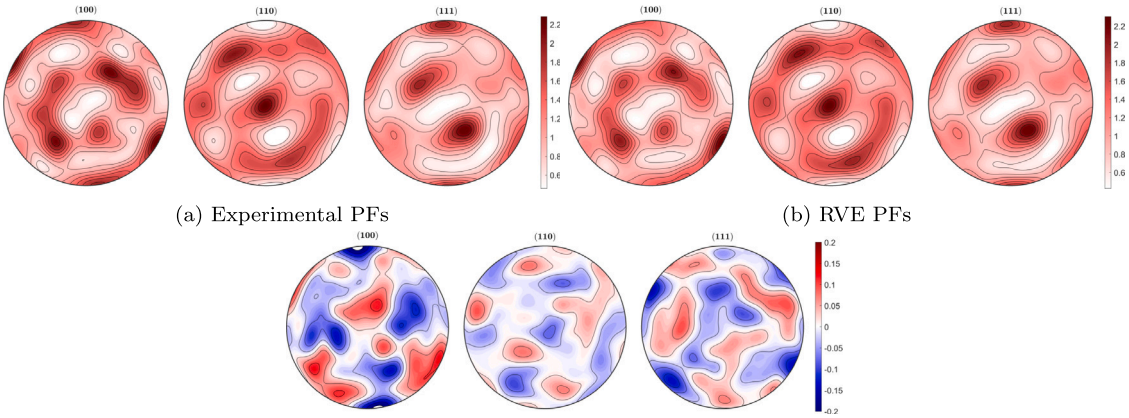

Fig. 8. Pole figures computed from the ODF of the experimental results (a) and the constructed RVE (b). The difference between pole figures is displayed in (c). (For interpretation of the references to color in this figure legend, the reader is referred to the web version of this article.)

where u_n^{sim} is the displacement at the location of node n and u_n^{exp} the (interpolated) experimental displacement at the same spatial location.

As seen from Eq. (5) only the pile-up, i.e. points with positive displacement, are taken into account and the actual indent is not compared. Disregarding the indent, whose topography directly depends on the shape of the indenter, ensures that the objective function is sensitive to the crystallographic orientation, which determines the pile-up topography. Through the optimization algorithm, CP parameters are being modified accordingly for every iteration.

First, the selection of the CP parameters is discussed in detail in Section 4.1 where also the assumptions made for each parameter are described. A study on the influence of element type and size on the simulated height profile is then given in Section 4.2. Third, the optimization algorithm is explained in depth in Section 4.3. Lastly, some technical details on how to evaluate the objective function are discussed in Section 4.4.

4.1. Selection of parameters

The CP model presented in Section 3 contains 38 parameters, of which alone 28 are required to populate the interaction matrix $q_{\alpha\alpha'}$ (cf [45]). Since it is not feasible to optimize in such a large parameter space, optimization needs to be limited to the parameters that have a high influence and whose values cannot be estimated. To this end, the known values are used for the following parameters:

- The initial hardening rate (h_0) is taken from Tasan et al. [27] where a fitting for the ferritic phase of the material using the same constitutive law was performed. This parameter accounts for the initial hardening when the plastic deformation begins, information which is extremely difficult to get from the imprint. Additionally, the effect on the final macroscopic stress–strain curve can be achieved with the other parameters that are fitted.
- The stress exponent n determines the rate sensitivity. It cannot be determined from experiments at a fixed deformation rate and is therefore taken from Tasan et al. [27] and kept constant.
- The reference shear rate $\dot{\gamma}_0$ is directly approximated from the nanoindentation load–displacement curves. The meaning of this parameter becomes apparent looking at Eq. (2): At the yield point, where $\tau^\alpha = \xi^\alpha$, the material is shearing with rate $\dot{\gamma}_0$ independently of the strain rate sensitivity. For this parameter, only the order of magnitude is relevant since the strain rate differs from slip system to slip system. Besides, due to the value of the stress exponent, stresses only change to a small amount for large changes in strain rate. Therefore, the slope of the displacement–time curve at the yield point (determined as the end of the linear elastic regime) is taken as the value for $\dot{\gamma}_0$.
- The components of the slip–slip interaction matrix ($q_{\alpha\alpha'}$) are assumed to be 1.4 for non-coplanar and 1.0 for coplanar interactions [46].

Table 2
Material parameters, based on Tasan et al. [27]. Parameters where a range is given are the ones to be fitted.

Property	Symbol	Value	Unit
Elastic constant	C_{11}	233.3	GPa
Elastic constant	C_{12}	135.5	GPa
Elastic constant	C_{44}	118.0	GPa
Initial resistance	$\xi^0_{\{110\}}$	(0, 97]	MPa
	$\xi^0_{\{112\}}$	(0, 88]	MPa
	$\xi^0_{\{123\}}$	(0, 83]	MPa
Saturation resistance	$\xi^\infty_{\{110\}}$	(97, 800]	MPa
	$\xi^\infty_{\{112\}}$	(88, 726]	MPa
	$\xi^\infty_{\{123\}}$	(83, 685]	MPa
Initial hardening rate	h_0	1.0	GPa
Reference shear rate	$\dot{\gamma}_0$	4.0	10^{-2}/s
Stress exponent	n	20.0	
Strain hardening exponent	a	(2, 20]	

The initial resistance of the slip plane families can be linked with the CRSS values measured experimentally for the micropillars. However, a direct use of these values is not possible, since the predicted yield point would be much higher than the experimental one due to size effects in micropillar compression experiments. Instead, these values are used as an upper bound limit. The lower bound is set to 0.0 MPa. Additionally, the experimentally obtained ratio between them, $\tau^{\text{crit}}_{\{110\}} : \tau^{\text{crit}}_{\{112\}} : \tau^{\text{crit}}_{\{123\}} \equiv 1 : 0.91 : 0.86$, is imposed as a constraint ($\xi^0_{\{110\}} : \xi^0_{\{112\}} : \xi^0_{\{321\}} \equiv 1 : 0.91 : 0.86$).

The saturation value of the CRSS cannot be determined from the micropillar compression experiments. Still, the ratios obtained for the initial CRSS are used to constrain these values as well ($\xi^\infty_{\{110\}} : \xi^\infty_{\{112\}} : \xi^\infty_{\{321\}} \equiv 1 : 0.91 : 0.86$). These constrains are motivated from the fact that the three plane families have similar packing density which results in similar Peierls stresses. Furthermore, the strain hardening mechanisms are similar for the 3 slip plane families. The lower bounds of these parameters are set according to the initial yield point as determined by the micropillar compression experiments. The upper bound is set to almost double of the maximum nominal stress in the stress–strain curve of the tensile test.

A summary of the material parameters, including elastic constants (C_{11}, C_{12}, and C_{44}), is shown in Table 2.

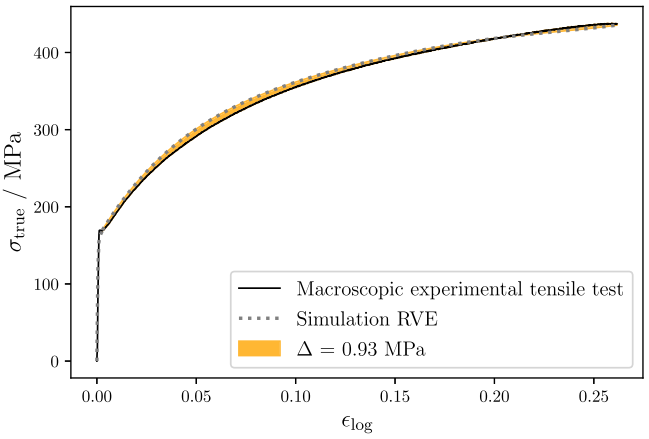

Fig. 9. Fitting from macroscopic tensile test.

Table 3
Parameters determined from fitting the macroscopic behavior.

Property	Symbol	Value	Unit
Initial resistance	$\xi^0_{\{1\,1\,0\}}$	76	MPa
	$\xi^0_{\{2\,1\,1\}}$	68	MPa
	$\xi^0_{\{3\,1\,1\}}$	65	MPa
Saturation resistance	$\xi^\infty_{\{1\,1\,0\}}$	277	MPa
	$\xi^\infty_{\{2\,1\,1\}}$	248	MPa
	$\xi^\infty_{\{3\,1\,1\}}$	237	MPa
Strain hardening exponent	a	2.0	

4.2. Selection of the mesh and the element type

The influence of the finite element mesh on the predicted force–displacement curve and pile-up topography is investigated. The goal is to determine the convergence limit, i.e. the mesh with the smallest number of elements that gives sufficiently accurate results. Since the study requires the use of reasonable material parameters, an initial guess of the material parameters is carried out. A direct fit using the macroscopic tensile test up to the ultimate yield stress (see Fig. 9) is done. The RVE (described in Section 3.2) is used for simulating the tensile test, and the parameters presented in Section 4.1 are manually adjusted until the resulting stress–strain curve matches the experimental one. The results of this identification are shown in Table 3. The error of the simulation stress–strain curve is measured by the area between the simulation and experimental curves (Δ).

The influence of the mesh resolution is studied for one crystallographic orientation (with Euler angles being $\phi_1 = 255.8°, \Phi = 75.9°, \phi_2 = 275.8°$ with the coordinate system as defined in Fig. 6). The different meshes presented in Table 1 are used for this analysis. The boundary conditions impose the experimental displacement shown in Fig. 4(c). Only the loading part (A to B) is analyzed here, while the holding and unloading part are not considered. Three different element types were considered for the study: a linear element with reduced integration, a linear element with full integration, a quadratic element with reduced integration. A quadratic formulation with full integration was also tested but discarded due to poor convergence. Simulations were run for combinations of all the meshes and element types, except for the two meshes with 81 920 and 129 024 elements, which were run only for the linear element with reduced integration due to the long computation time when using the other element types. The load–displacement curves are displayed in Fig. 10. Some curves are not shown with the purpose of a better visualization. The continuous line corresponds to the mesh with the highest number of elements and is considered the most accurate result. The line made of square markers corresponds to the mesh with the minimum number of elements that still resulted in a converged stress–strain curve. For a converged result, a threshold of $\approx 0.012\,\mu$N is established for the mean absolute error with respect to the most accurate solution. When using the linear element with reduced integration (see Fig. 10(a)), a mesh of 81 920 elements has to be used to reach convergence. In contrast, for the linear element with full integration (see Fig. 10(b)), a mesh of 10 240 elements suffices to reach convergence and for the quadratic element with reduced integration (see Fig. 10(c)), a mesh of only 2 016 elements can be used to reach convergence.

A mesh sensitivity analysis was also done regarding the topography. The maximum height of the pile-up is chosen as an indicator for this analysis and is plotted in Fig. 11. Fig. 11(a) shows the results for different meshes and element types. For the linear element with reduced integration, the maximum height is underestimated when using a small number of elements. As the number of element is increased, the maximum height increases. However, it is not clear whether mesh convergence has been reached even for the finest mesh with 129 024 elements. The results shown in Fig. 11(d) indicate that the mesh type does not play an important role for linear elements with reduced integration, and the general trend is maintained regardless of the base mesh used. For the linear element with full integration, the maximum height is overestimated when using a small number of elements. For this case, base mesh A with 424 and 3 392 elements shows big deviation from the reference result (see Fig. 11(b)). The quadratic element with reduced integration showed stability and quick convergence, in agreement with the sensitivity analysis of the stress–strain curve (see Fig. 11(c)).

The time for the simulations is displayed in Fig. 12. A horizontal black dashed line is plotted to indicate a threshold line for 24 h. Above this mark, simulations are considered too time demanding for use in the optimization procedure. It can be seen that the run times of the linear element with full integration and the quadratic element with reduced integration are similar. This is explained by the fact that both elements have the same number of integration points (8) and thus constitutive evaluations, which are the main contributors to the run time. For the linear element with reduced integration (single integration point), the time is significantly lower compared to the other two element types.

For selecting a combination of mesh and element type, it must perform adequately in terms of convergence of the load–displacement curve (Fig. 10), convergence of the topography (Fig. 11), and in time efficiency (Fig. 12). Taking this into account, the mesh with 2 016 quadratic elements with reduced integration was selected. This combination of mesh and element type shows convergence of the load–displacement curve and the topography at a run time of only four hours.

The selected combination of mesh and type of element was also tested for a second orientation (with Euler angles being $\phi_1 = 145.1°, \Phi = 51.0°, \phi_2 = 223.8°$). It was directly compared against the high resolution mesh with 54 432 elements. Both criteria – load–displacement and topography – exhibited better convergence (not shown) than for the other orientation. In Fig. 13, the results for the selected mesh and element type and a higher resolution mesh with the same element type is shown for both orientations. It becomes apparent that the pile-up pattern is well captured in both cases using the coarse mesh.

4.3. Optimization algorithm

The minimization problem consists of finding the global minimum of a multivariate, non-linear, and continuous function. Often, gradient-based methods like the Nelder–Mead method are being used for inverse modeling. The biggest limitation of these methods is their strong dependency on the starting point [47]. A global minimum will be found only if a suitable initial guess is used. Otherwise, the algorithm converges to a local minimum. In the case of material parameters, a good initial guess is not always possible, and therefore gradient-based methods are not ideal. In order to find the global minimum, other types of algorithms such as the differential algorithm developed by Storn and

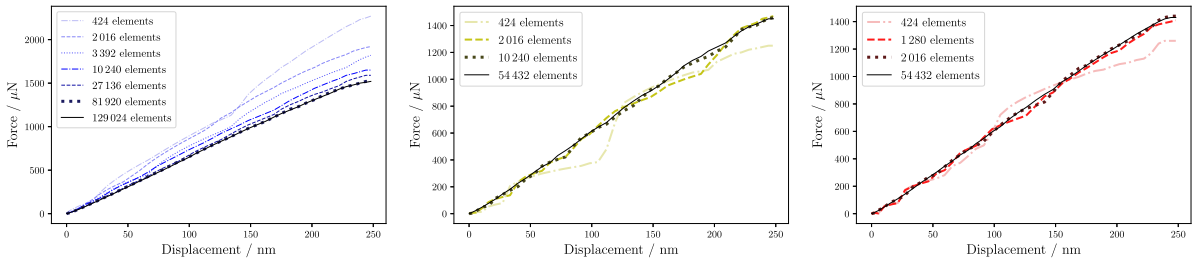

(a) Linear element with reduced integration

(b) Linear element with full integration

(c) Quadratic element with reduced integration

Fig. 10. Load displacement curves for different element types (a, b, c) and meshes with different numbers of elements.

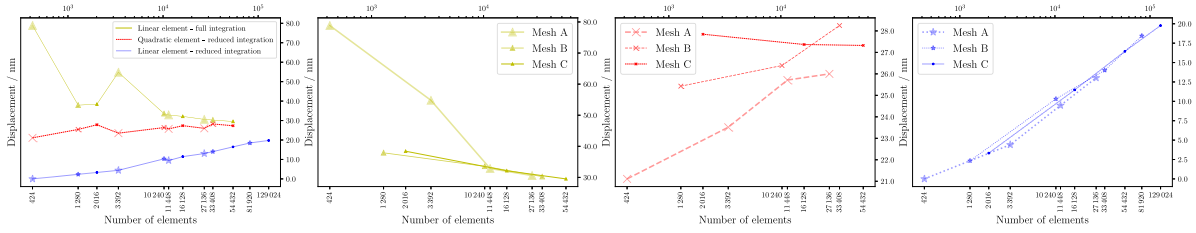

(a) Different meshes and element types

(b) Linear element with full integration

(c) Quadratic element with reduced integration

(d) Linear element with reduced integration

Fig. 11. Maximum height of the pile-up pattern for different meshes and element types.

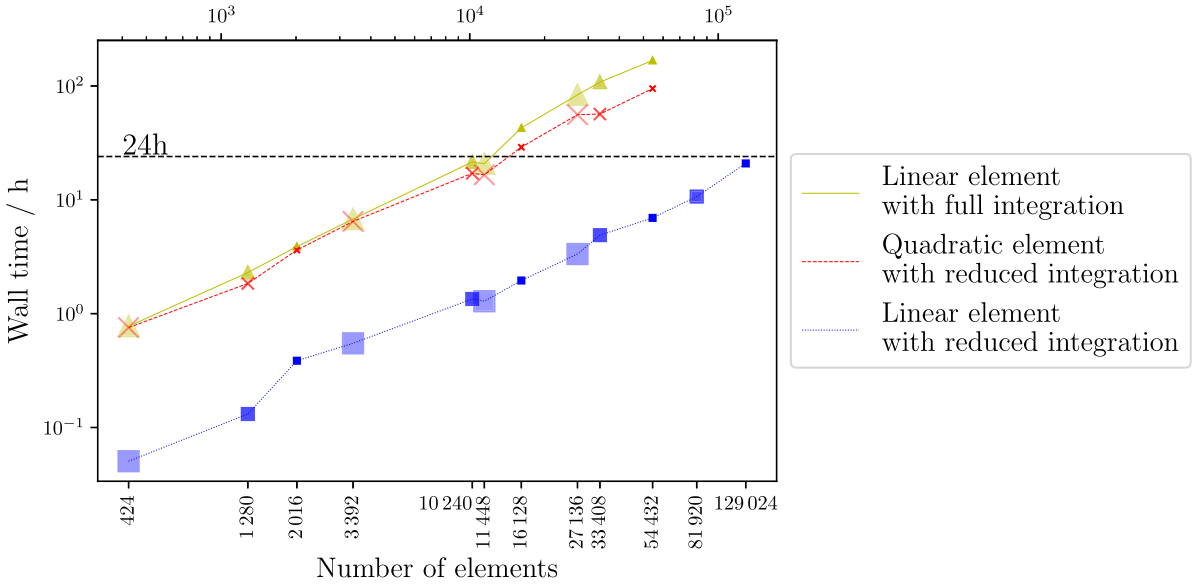

Fig. 12. Wall time of the simulations for different meshes and element types.

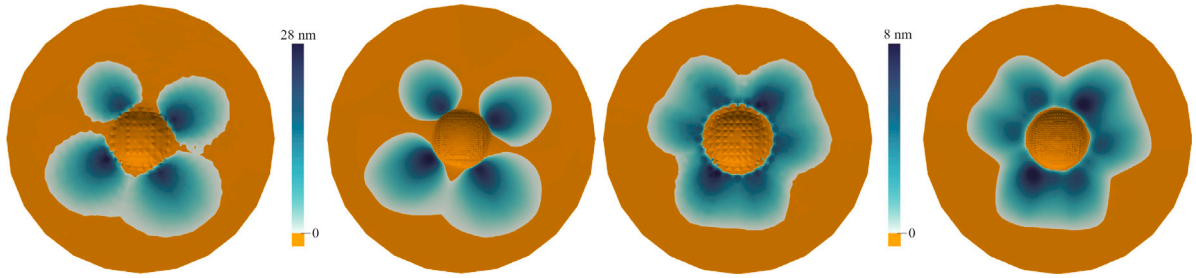

(a) Orientation I ($\phi_1 = 255.8°, \Phi = 75.9°, \phi_2 = 275.8°$).

(b) Orientation II ($\phi_1 = 145.1°, \Phi = 51.0°, \phi_2 = 223.8°$).

Fig. 13. Results for the selected coarse mesh (left) and a high resolution mesh (right) for the two orientations used for the convergence study. (For interpretation of the references to color in this figure legend, the reader is referred to the web version of this article.)

Price [48] are better suited. In contrast to gradient-based approaches, these methods use stochastic processes which makes it possible to scan large areas of the parameter space. As a drawback, they require more function evaluations than conventional gradient-based techniques. The algorithm is based on iteratively improving a candidate solution based on an evolutionary process. Since this method offers many possibilities to vary it (selection of initial population, strategy for mutation, etc.), the discussion in the following is limited to the differential evolution (DE) approach used here.

The algorithm is first initiated with a population of N candidate solutions, each of which is described by a vector of length L corresponding to the number of parameters to be optimized. The selection of this population is made through 'latin–hypercube' sampling originally formulated by Tang [49]. It is a statistical technique for obtaining a near-random sample of parameter values from a multidimensional distribution. This population evolves during each generation, represented by $G = 0, 1, \dots, G_{\text{final}}$, until a final one is reached. Thus, candidate i of the N candidate solutions of generation G is represented by

$$\Xi_i^G = \left[\varrho_{1,i}^G, \varrho_{2,i}^G, \dots, \varrho_{L,i}^G\right] \tag{6}$$

In the DE algorithm, this vector is called target. A donor vector θ is calculated from a mutation of the current target vector. There are several strategies for the mutation. Here, the 'best1bin' strategy is used. For each generation, the best solution is denoted by Ξ_{best}^G. The donor vector is then obtained by

$$\theta_i^G = \Xi_{\text{best}}^G + \underbrace{F}_{\in[0,2]}\left(\Xi_{r_1^i}^G - \Xi_{r_2^i}^G\right) = \left[\theta_{1,i}^G, \theta_{2,i}^G, \dots, \theta_{L,i}^G\right] \tag{7}$$

where r_1^i and r_2^i are different target vectors randomly chosen and F is the mutation factor (also called differential weight) with a value between 0 and 2. In this case, random dithering is employed, and F changes for every generation. The parameters in the donor vector ($\theta_{1,i}^G$) must satisfy the bounds. Otherwise, the donor vector is recalculated. A crossover operation is applied after mutation to obtain a trial vector Γ_i^G. This is done by the exchange of variables between target and donor with a binomial distribution based on a random number $R \in (0, 1]$ that is generated. It is then compared to the recombination constant, also known as the crossover probability or the crossover constant and denoted as $R_{\text{threshold}}$ (in our case, $R_{\text{threshold}} = 0.7$) for selecting the l^{th} parameter from either the target vector or the donor vector. The last parameter is always chosen from the donor vector.

$$\Gamma_i^G = \left[\gamma_{1,i}^G, \gamma_{2,i}^G, \dots, \gamma_{L-1,i}^G, \theta_{L,i}^G\right], \text{ with } \gamma_{l,i}^G := \begin{cases} \varrho_{l,i}^G & \text{if} \quad R \geqslant R_{\text{threshold}} \\ \theta_{l,i}^G & \text{else.} \end{cases} \tag{8}$$

The trial vector is then evaluated. If it is a better solution than the target vector, it substitutes it for the next generation. If not, the target vector is kept as part of the population for the next generation.

The numerical algorithm used is the one implemented in the SciPy Python library [50].

4.4. Evaluation of the objective function

To compare the experimental and simulated results, two technical details must be tackled: the alignment of the experimental and simulated imprints and the interpolation strategy to calculate the experimental and simulated displacements at the same positions.

Regarding the alignment, firstly, the center position of both, experimental and simulated images, is lined up. The experimental center is assumed to coincide with the pixel with the lowest height (see Section 2.6). The simulation center is taken as the central node, which coincides with the first node in contact (even after the sample is tilted). This is indicated by a black cross in Fig. 15. The remaining rotational degree of freedom is fixed by aligning the maximum height obtained from the simulation (Fig. 13) with the experimental maximum height. This results in the alignment of the experimental and simulation pile-up patterns. Since the CRSS ratio of the slip plane families is kept constant (it is the same as for the mesh sensitivity analysis in Section 4.2 and for the optimization in Section 5.1), it is expected that the axial positions of the pile-up maxima remain unchanged.

Secondly, an interpolation strategy must be chosen for the calculation of the objective function (λ in Eq. (5)). The experimental topography exists on a regular 512×512 pixel grid and displacements are measured at the center of each pixel denoted by i. The simulation outputs the topography on an irregular mesh and displacements are calculated at the nodes denoted by n. Here, the experimental data (u_i^{exp}) is mapped to the irregular mesh of n nodes of the simulation using Gaussian interpolation. Since all nodes are equally weighted in Eq. (5), the denser areas of the irregular mesh – closer to the center – are given more importance than those with lower nodal density. The calculation of the experimental interpolated value on the node n reads:

$$u_n^{\text{exp}} = \overbrace{\sum_i w_i}^{=1} \sum_i u_i^{\text{exp}} = C \cdot \sum_i u_i^{\text{exp}} e^{\left(\frac{-s \cdot r_i}{\text{R}}\right)}, i \text{ being nodes with } r_i \leqslant R \tag{9}$$

where r_i is the distance from the experimental point to the node n, s is the sharpness, which controls the rate of decay of the Gaussian and R is the maximum distance from node n for which experimental points i are taken into account for interpolation. For the optimization procedure in Section 5.1, R = 15 nm is used. An in-depth analysis of this selection is carried out in Section 5.3 where also other radii are used to calculate the experimental interpolated topography. The interpolation methods, as implemented in VTK [51,52], are used via PyVista [53].

5. Results

First, the details of the optimization procedure for determining the CP parameters are given in Section 5.1. The outcome without the constraints from the micropillar experiments is presented in Section 5.2. Third, an analysis of the interpolation strategy is detailed in Section 5.3. Finally, the effect of the friction and the tilt angle is discussed in Sections 5.4 and 5.5, respectively.

5.1. CP parameters from optimization procedure

Two indents with different orientations are considered for this study. Indent I and indent II correspond to the orientations of Euler angles $\phi_1 = 255.8°, \Phi = 75.9°, \phi_2 = 275.8°$ and $\phi_1 = 145.1°, \Phi = 51.0°, \phi_2 = 223.8°$, respectively. The two orientations are the same ones for which the mesh sensitivity analysis was done in Section 4.2. The optimization algorithm is carried out independently for each of them. Only the loading and holding part (A-C) is considered whereas the unloading part (C-D) is ignored (c.f. Fig. 4).

A single population (N = 10) is evaluated once in every iteration. Fitting the seven parameters requires to optimize three independent variables (L = 3) after imposing the constraints from the micropillar experiments. The value λ of the objective function, Eq. (5), is determined in total 420 times (42 generations) per indent and its evolution is shown in Fig. 14. The objective function of indent I reaches its minimum value of $\lambda = 11.1$ nm at $G = 31$ (see Fig. 14(a)). As shown in Fig. 14(b), a minimum value of $\lambda = 10.4$ nm is reached at $G = 35$ for indent II. The best solution at each generation (Ξ_{best}^G) is marked and labeled with their CP parameters. For each set of CP parameters, a simulated tensile test of the RVE presented in Section 3.2 is done to simulate the macroscopic bulk behavior and the difference between the stress–strain curve obtained with the given set of CP parameters and experimental macroscopic tensile test is measured by the area between

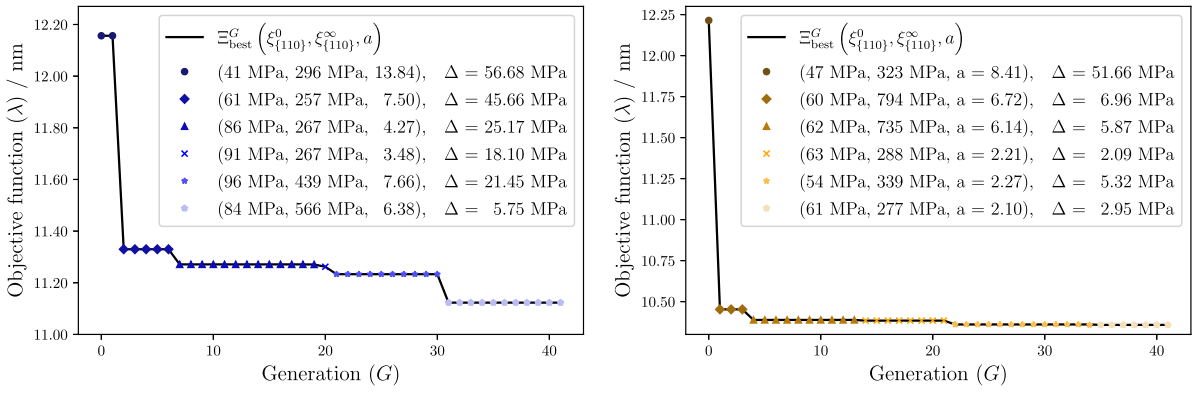

(a) Indent I (b) Indent II

Fig. 14. Evolution of the objective function (λ) across the generations in the optimization procedure.

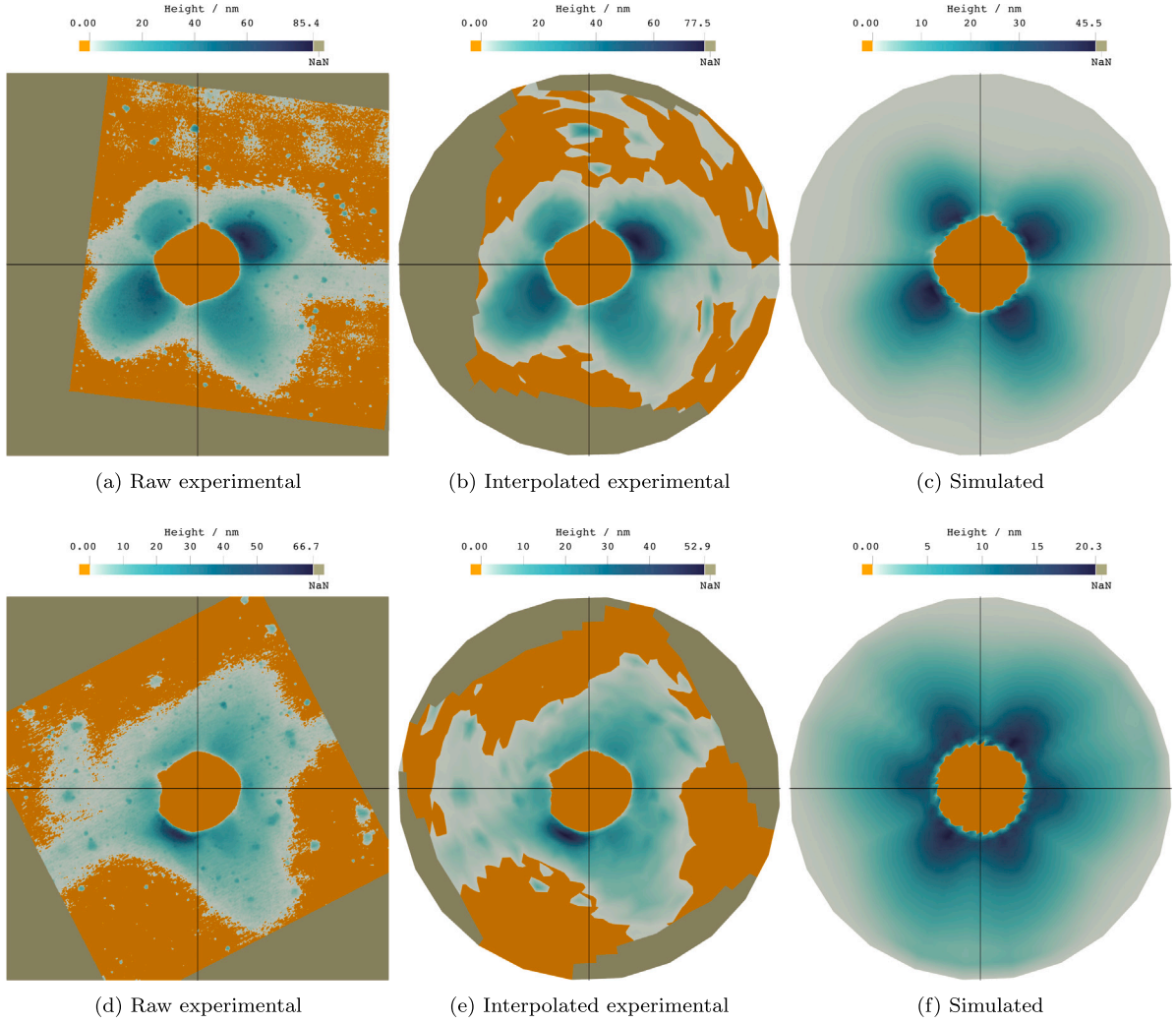

(a) Raw experimental (b) Interpolated experimental (c) Simulated

(d) Raw experimental (e) Interpolated experimental (f) Simulated

Fig. 15. Comparison of the raw experimental (left), interpolated experimental (center), and simulated (right) imprints for indent I (top row) and indent II (bottom row). (For interpretation of the references to color in this figure legend, the reader is referred to the web version of this article.)

them (Δ). For both indents a decrease in Δ is observed for a decrease of λ.

The optimized CP parameters determined from each indent and from the direct fitting in Section 4.2 are used to simulate the macroscopic bulk behavior. To this end, the RVE presented in Section 3.2 is used. For each set of CP parameters, a simulated tensile test of the RVE is done and the difference between the stress–strain curve obtained with the given set of CP parameters and experimental macroscopic tensile test is measured by the area between them (Δ).

Once the optimized CP parameters are determined, a simulation that includes the unloading part (C-D) is performed for each indent to enable an extended comparison with the experiments. The results are

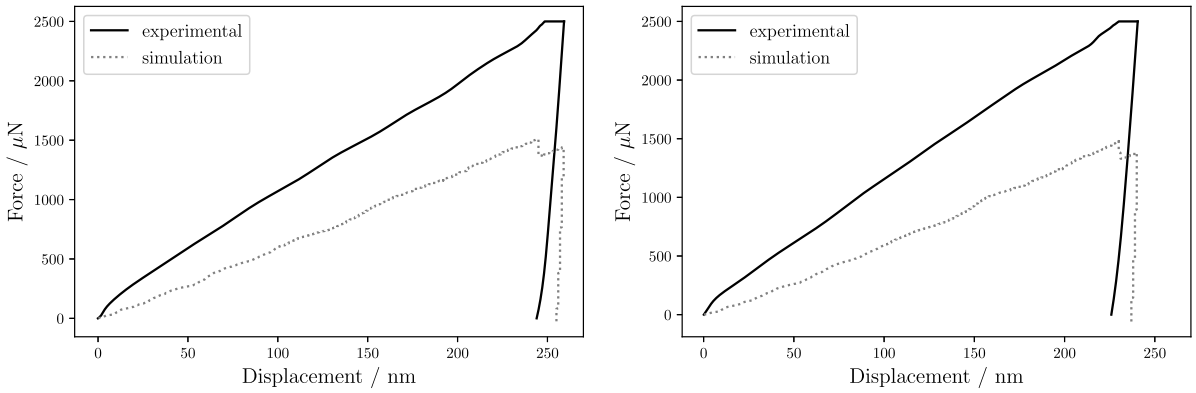

(a) Load–Displacement curve of indent I (b) Load–Displacement curve of indent II

Fig. 16. Comparison of the load–displacement curves coming from the simulation with optimized CP parameters and the experiments.

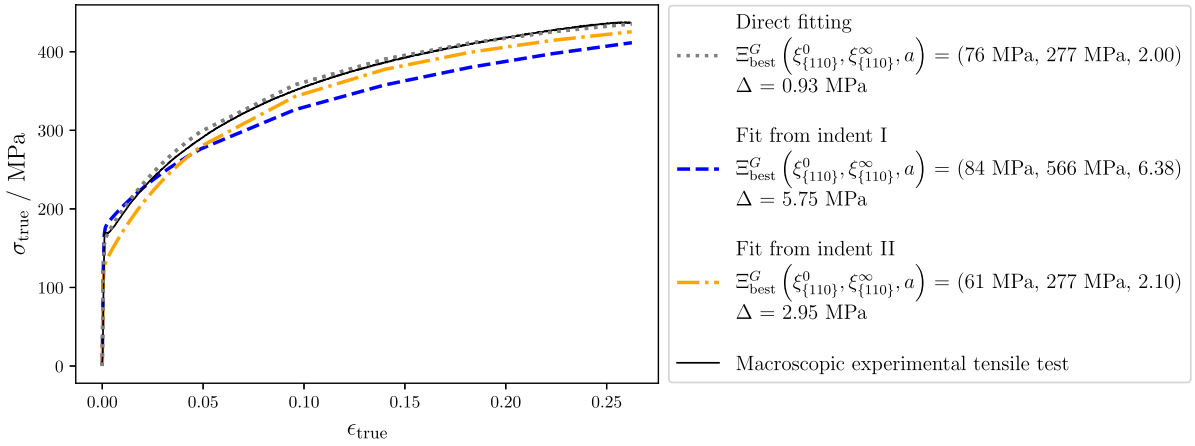

Fig. 17. Simulated bulk behavior using the CP parameters determined from the direct fitting and the fits from the indents.

displayed in Fig. 15, for which the top row corresponds to indent I and the bottom row to indent II. The raw experimental topography (left) is displayed in the original rectilinear grid from the AFM measurements. The interpolated experimental topography (center) and the simulated one (right) are displayed in the corresponding mesh used for the simulation. The color orange indicates heights below 0 nm and therefore are not part of the pile-up zone considered here. The gray color corresponds to zones where the interpolation cannot not be performed and it is labeled as 'not a number'. For indent I, the raw experimental topography (see Fig. 15(a)) exhibits an almost 4 fold symmetry which is broken since the 4 maxima are not identical and have very different values. Starting from the biggest pile-up on the right-top corner and going clock-wise, the heights are 85.4 nm, 35.1 nm, 51.0 nm, and 32.1 nm. For the interpolated topography (see Fig. 15(b)), the heights are 77.7 nm, 34.9 nm, 49.7 nm, and 29.8 nm. In the simulated imprint (see Fig. 15(c)), the topography is closer to a strict 4-fold symmetry with the heights of the maxima being 45.5 nm, 39.4 nm, 42.6 nm, and 41.1 nm. For indent II, the raw experimental topography (see Fig. 15(d)) exhibits 6 maxima and appears to have a 6-fold axis of rotational symmetry if considering only the positions of these maxima. Starting from the biggest pile-up in the bottom left and going clock-wise, the heights of the maxima for the experimental imprint are 66.7 nm, 20.6 nm, 21.1 nm, 26.2 nm, 28.5 nm, and 26.3 nm. For the interpolated topography (see Fig. 15(e)), the heights are 52.9 nm, 17.8 nm, 19.2 nm, 23.3 nm, 22.4 nm, and 24.6 nm. The symmetry becomes more apparent for the simulated imprint (see Fig. 15(f)) where the heights are 20.3 nm, 15.7 nm, 17.2 nm, 19.0 nm, 16.6 nm, and 17.7 nm.

In Fig. 16, the load–displacement curves are displayed for indents I and II, respectively. The boundary conditions for the simulation impose the experimentally measured displacement although the experimental nanoindentation was load-controlled. This is the cause of the sudden drop in load for the holding part (B-C). It is important to note that these curves are not used for the optimization procedure. In both cases, the simulated nanoindentation predicts a softer material in the microscopic regime since the final displacement is achieved with about half of the experimental load. This is discussed later on in Section 6.2.

The optimized CP parameters determined from each indent and from the direct fitting in Section 4.2 are used to simulate the macroscopic bulk behavior. The results are shown in Fig. 17. The experimental yield point of 170 MPa is overestimated by the fit from indent I (179 MPa) while it is significantly underestimated by the fit from indent II (130 MPa) compared to the direct fitting (168 MPa). The experimental stress at the final deformation of 438 MPa is underestimated by the fit from indents I and II (410 MPa and 423 MPa, respectively) compared to the direct fitting (435 MPa). The Δ parameter is found to be greater for the fits from indent I (5.75 MPa) and indent II (2.98 MPa) compared to the direct fitting (0.93 MPa)

5.2. Effect of the constraints from the micropillar experiments

In Section 5.1, constraints from the micropillar compression experiments – the upper bounds and the ratios of the three slip plane families – are used. Here, the optimization procedure is carried out without these constraints. In this case, the initial and saturation resistances are bounded from 0 MPa to 800 MPa. Additionally $\xi_i^0 < \xi_i^\infty$ for the three slip plane families $i = 1,3$ is imposed. The evolution of the objective function (λ) across the generations with and without

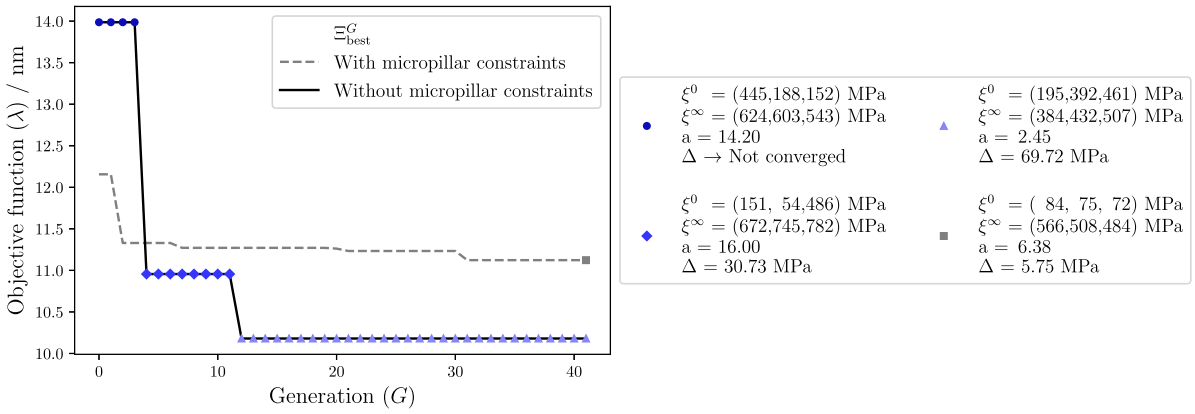

(a) Indent I

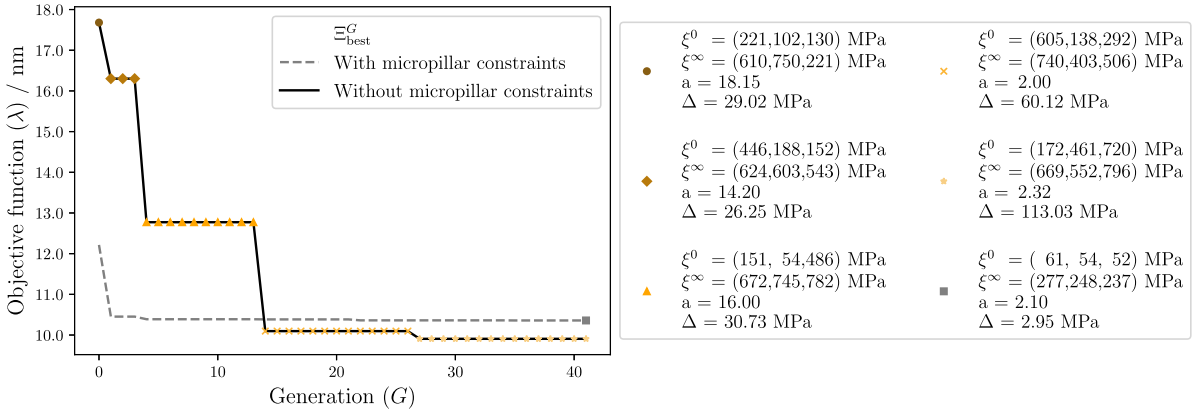

(b) Indent II

Fig. 18. Evolution of the objective function (λ) across the generations with and without the constraints from the micropillar compression experiments.

constraints from the micropillar experiments is shown in Fig. 18. It can be seen that the objective function has higher values at the beginning of the optimization procedure compared to the situation with the micropillar constraints. However, the optimization procedure without the micropillar constraints is already outperforming the other one at $G = 5$ (with $\lambda = 10.9$ nm) for indent I and at $G = 14$ (with $\lambda = 10.1$ nm). At the end, the objective function optimized without the micropillar constraints reaches the values of $\lambda = 10.2$ nm and $\lambda = 9.9$ nm for indents I and II, respectively. The value of Δ, a measure for the difference between the experimental and simulated stress–strain curve, is also displayed in Fig. 18 for each set of CP parameters. Interestingly, in contrast to what was seen in Section 5.1, the minimization of λ is not correlated with a better prediction of the macroscopic bulk behavior. This is clearly illustrated for indent II, where Δ rises as the minimization takes place: 29 MPa, 26 MPa, 31 MPa, 60 MPa, and 113 MPa.

The macroscopic behavior predicted by the set of the CP parameters determined with and without using the constraints from micropillar compression are shown in Fig. 19. The fits from both indents without the constraints do not represent the experimental bulk mechanical behavior with yield points around 500 MPa which is almost 2.7 times higher then the experimental one. The fit from indent I predicts a stress of approximately 600 MPa at the final deformation compared to the experimental one of 438 MPa, while the fit of indent II predicts a stress of almost 1000 MPa.

5.3. Effect of the interpolation strategy

The effect of the interpolation strategy on the results in Section 5.1 is analyzed. To this end, the radius R used in the Gaussian interpolation is changed to obtain different experimental interpolated values u_n^{exp} (see Eq. (9)). The objective function (λ in Eq. (5)) is then re-evaluated for the already existing completed simulations in Section 5.1 (420 for each indent). The best solution (Ξ^G_{best}) is plotted for different radii against the Δ parameter for indent I in Fig. 20. The range where Ξ^G_{best} is stable is highlighted in green and corresponds to a radius of 7 nm to 60 nm. Outside that zone, the obtained CP parameters cannot be used for representing the macroscopic bulk behavior of the material since there is a large deviation of more than 15% on the stress–strain curve. For indent II (not shown) the stable solution is in the range of 9 nm to 38 nm.

5.4. Effect of friction

Simulations using the obtained CP parameters (Section 5.1) with different friction coefficients are run to analyze the effect of the friction on the simulation results. It is important to note that the load–displacement curves as well as the sink-in part of the topography are analyzed even though they were disregarded in the optimization procedure in Section 5.1 (c.f. Eq. (5)).

The load–displacement curves for different friction coefficients are shown in Fig. 21. The figures for indent I (Fig. 21(a)) and II (Fig. 21(b)) are displayed with a zoom-in on the last part of the curve where the largest deviations appeared. For lower friction, less load is needed to achieve the same displacement. The maximum load for indent I is 1510 μN, 1490 μN, 1460 μN, and 1420 μN for values 0.3, 0.18, 0.1, and 0.01 of the friction coefficient. Above $\mu = 0.3$, saturation happens, and results for $\mu = 0.4$, and $\mu = 0.5$ are almost identical. The maximum load reached for indent II is 1500 μN, 1480 μN, 1460 μN, 1410 μN, and 1360 μN friction coefficients of 0.5, 0.3, 0.18, 0.1, and 0.01.

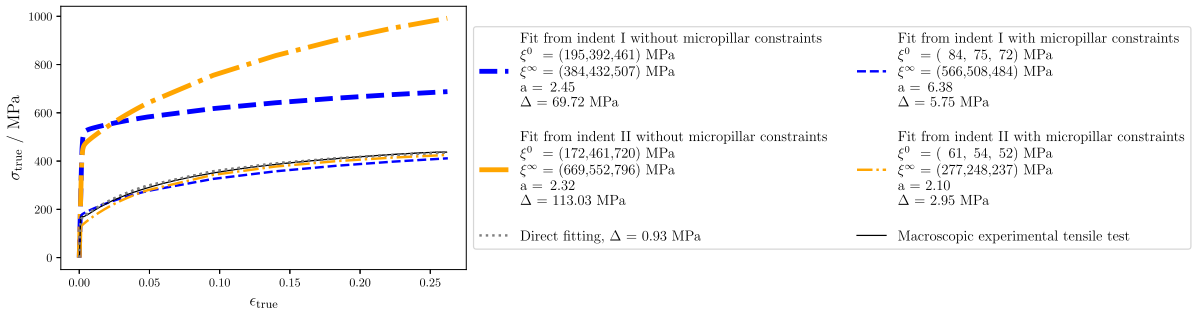

Fig. 19. Simulated bulk behavior using the CP parameters determined from the direct fitting and the fits from the indents with and without the constraints from the micropillar compression experiments.

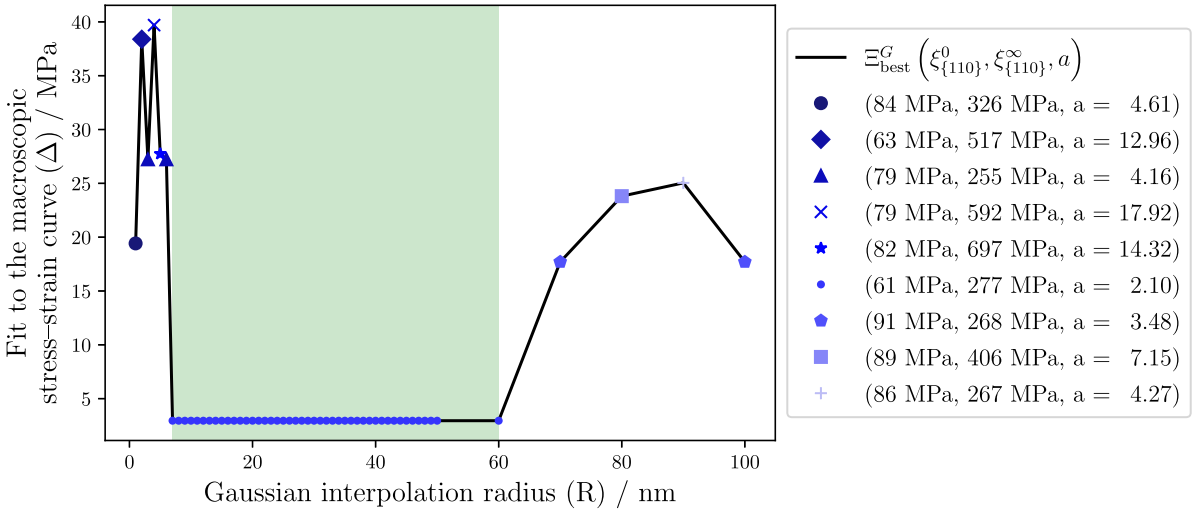

Fig. 20. CP parameters determined from indent I by using different radii in the interpolation strategy to calculate the experimental interpolated topography. (For interpretation of the references to color in this figure legend, the reader is referred to the web version of this article.)

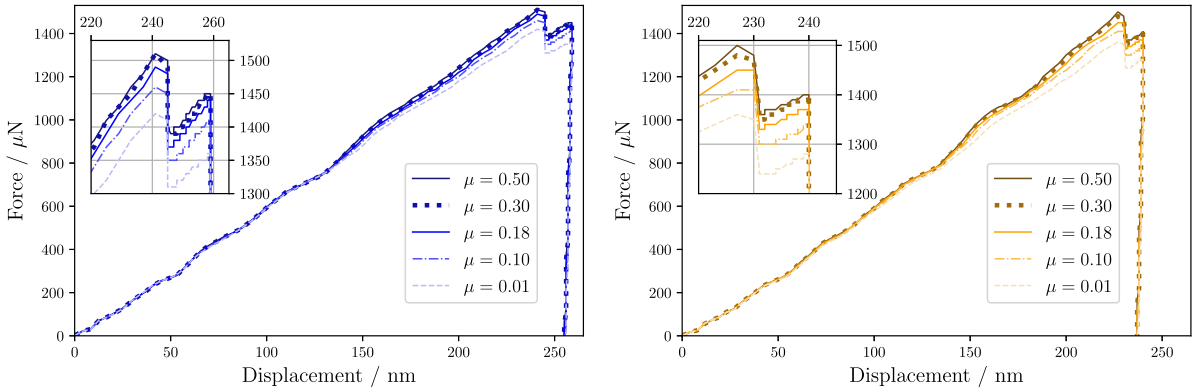

(a) Indent I (b) Indent II

Fig. 21. Effect of the friction coefficient on the load–displacement curve.

The effect of friction on the topography is displayed in Fig. 22 where the maximum sink-in depth (Fig. 22(a)) and the maximum pile-up height (Fig. 22(b)) are displayed for different friction coefficients. The maximum sink-in depth (H_{min}) is measured at the end of the simulation and it is normalized by the experimental maximum depth (H^{exp}_{min}), which is 260 nm for indent I and 240 nm for indent II. For low friction, H_{min} is greater than the experimental one and it decreases in absolute value towards the experimental value till approximately $\mu = 0.3$ where saturation happens. The largest maximum height of the pile-up (H_{max}) is also measured at the end of the simulation and it is normalized by the experimental maximum height (H^{exp}_{max}), which is 85 nm for indent I and 67 nm for indent II. The maximum value of H_{max} is obtained for the lowest μ and then decreases when increasing the friction coefficient.

5.5. *Effect of the surface tilt*

To analyze the effect surface misalignment on the simulation results, simulations using the determined CP parameters are run for tilt angles θ in the range 0° to 5°. To limit the parameter space, the alignment of

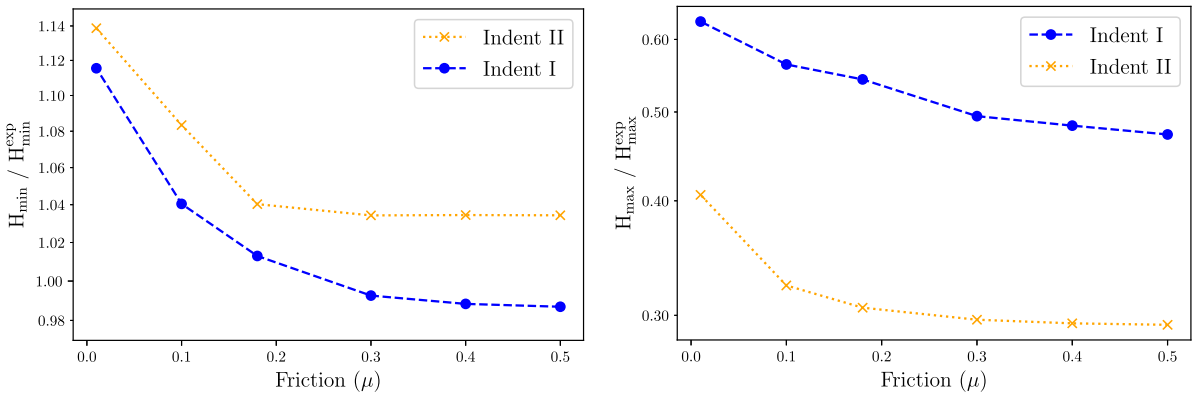

(a) Maximum sink-in depth (b) Maximum pile-up height

Fig. 22. Effect of the friction coefficient on the topography output of the simulations.

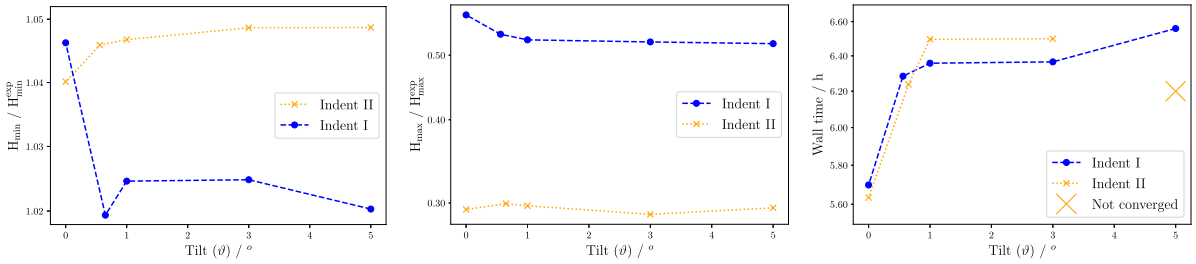

(a) Maximum sink-in depth (b) Maximum pile-up height (c) Wall time of the simulations

Fig. 23. Effect of the tilt (ϑ) on the topography output and on the wall time of the simulations.

the tilt axis is fixed, i.e. φ in Fig. 6(b) remains at the experimentally obtained value. As for the study on the influence of friction (Section 5.4), the load–displacement curves as well as the sink-in part of the topography are included in the analysis.

The load–displacement curves (not shown) are not significantly affected by the tilt for both indents. A maximum deviation of 30 MPa is observed approximately at the maximum indentation depth.

The analysis of the topography is done as in Section 5.4 but without the unloading part (C-D) because some simulations did not converge in the unloading regime. The results are shown in Fig. 23. The maximum sink-in depth (Fig. 23(a)) does not change significantly — the variation of the ratio H_{min}/H^{exp}_{min} is within a range of 0.03 and 0.01 for indents I and II, respectively. The maximum pile-up height (Fig. 23(b)) is almost constant for indent II for all values of the tilt angle. In contrast, for indent I, the ratio is higher (0.57) for the non-tilted sample compared to the tilted ones (0.53). The wall time of the simulations is displayed in Fig. 23(c). The simulations using non-tilted samples require less time than those with tilted surface. The maximum times are obtained for the maximum tilt for both indents. The simulation for indent II and a tilt of 5° was not able to be completed due to convergence issues.

6. Discussion

The presented method for determination of CP parameters by inverse modeling is discussed with respect to the choices and simplifications made for modeling and experiments. The influence of several investigated effects on the accuracy and robustness is then explained, followed by comments on general aspects regarding the nano to macro scale transition. Finally, the application of the method to multi-phase materials is outlined.

6.1. Choices and simplifications made

Neglecting the unloading part. During the optimization in Section 5.1, the unloading part of the load–displacement curve (C-D) was neglected due to severe convergence issues. Convergence is difficult to reach whenever the indenter and the sample lose contact. During the unloading part, this can happen several times at different positions which creates a large source of numerical instability. For the optimized parameters, a complete simulation was done including the unloading part, but a stricter convergence criterion was imposed at the cost of a longer simulation time. For indent I, the maximum height of the pile-up, not taking into account the unloading part is 44.7 nm for both values of the convergence criterion. For the complete simulation with the stricter convergence criterion, a maximum height of 45.5 nm was obtained. For indent II, the maximum height of the pile-up, not taking into account the unloading part, is 20.1 nm for both values of the convergence criterion. For the complete simulation with the stricter convergence criterion, a maximum height of 20.3 nm was obtained. From these results, the conclusion that both convergence criteria output similar results can be drawn. Also, when taking into account the unloading part, the maximum height in the pile-up area was increased by 1.8 % and 1.1 % for orientation I and II, respectively. Looking at the comparison of pile-up patterns given in Section 5.1, this small difference is not expected to have a huge impact on the overall result.

Constraints from the micropillar compression experiments. Running the parameter identification without the constraints obtained the micropillar compression experiments results in lower values for the objective function λ in comparison to the proposed approach of using these constraints (Section 5.2). However, in this case the minimization of λ does not go together with the determination of CP parameters that

accurately represent the macroscopic behavior. The determined CP parameters without constrains predict bulk behavior that is significantly harder than the experimental reference. From this results, the conclusion that the micropillar experiments are necessary – and not just helpful in reducing the independent variables to be determined – to get reliable and usable CP parameters for the macroscopic regime can be drawn.

Interpolation strategy. The calculation of the loss function requires an approach for interpolation of the experimentally measured displacement values to the nodal positions of the simulation mesh (u_n^{exp} in Eq. (9)). For the results presented in Section 5.1, Gaussian interpolation with cutoff radius R = 15 nm was used for this purpose. In Section 5.3 the consequences of using different radii for the interpolation strategy are presented. The results show that low and high values for R result in different minima for the objective function λ and, accordingly, correspond to different sets of CP parameters. However, there exists a wide range for the radius of the interpolation (7 nm to 60 nm for indent I and 9 nm to 38 nm for indent II) where the minimum is the same and the obtained parameters predict the macroscopic bulk behavior in good agreement with the experiment. Outside this ranges, the obtained CP parameters do not correctly reproduce the macroscopic bulk behavior of the material. For small radii, the interpolation is very sensible to artifacts in the AFM data such as dirt on the sample. For large radii, it is hypothesized that the sink-in part alters the topography of the pile-up pattern in two different ways: First, the total number of u_n^{exp} with a height greater than 0, N_{active}, changes — $N_{\text{active}} = 610$ for R = 15 nm whereas $N = 594$ for R = 100 nm for indent I and $N_{\text{active}} = 581$ for R = 15 nm whereas $N_{\text{active}} = 576$ for R = 100 nm for indent II. Second, the topography itself is changed. An example of this is the difference in the maximum pile-up height. For indent I, 77.53 nm is obtained for R = 15 nm whereas 75.41 nm is obtained for R = 100 nm. For indent II, 52.91 nm is obtained for R = 15 nm whereas 51.29 nm is obtained for R = 100 nm. This alterations are explained by the fact that, although the Gaussian interpolation puts more weight on the points closer to the node being interpolated, the maximum depths — 260 nm and 240 nm — are changing the interpolated pile-up area significantly since they were larger than the maximum heights — 85 nm and 67 nm for indents I and II, respectively.

Friction. It is assumed that the friction between the indenter and the sample can be modeled using Coulombs friction law with $\mu = 0.18$. Most of the models in literature also assume this, when friction between a diamond tip and steel is considered, with μ ranging from 0 in some frictionless models [29,54] up to 0.3 in others [55]. However, in that range, 0 , to 0.3 , the topography changed significantly in this study (see Fig. 22). Consequently, the use of a different value of μ will lead to a different result of the optimization. The method is therefore dependent on having a reliably parameterized friction model.

Surface tilt. The incorporation of the experimentally measured tilt into the nanoindentation modeling does not have a relevant impact neither for $\vartheta = 0.56°$ (indent I) and nor for $\vartheta = 0.65°$ (indent II). However, it significantly deteriorates the convergence and entails an increase in the simulation time (see Section 5.5). For properly set up indentation experiments ($\vartheta < 5°$) the tilt may be neglected in the simulation.

Indenter tip. It is possible to measure the tip shape to include that as part of the modeling, but this was not done here. The indenter was used for the first time after purchase for this experiment, and so the tip was assumed to have the exact shape as described by the manufacturer.

The size and the tip of the indenter was selected based on two criteria: On the one hand, a small tip is needed since a possible application of this method are steels made of complex microstructures with small features, i.e. martensitic laths or bainitic sheaves. The ability to hit single orientations in such application cases is proportional to the indenter dimensions. On the other hand, an effort is done to minimize the indentation size effects that describe the increase in hardness with decreasing size of the indent. For that reason, a smaller indenter could not be used since indentation size effects would not be negligible. In addition, a spherical tip was chosen, as more shallow indents are known to exhibit a more significant indentation size effect [56]. Furthermore, the spherical shape offered other advantages which are explained in what follows [24]. Several studies show the importance of using different indenter shapes to increase the accuracy and remove ambiguity that is likely to result from comparison between experiment and model for a single shape in the determination of parameters obtained from inverse modeling [57–59]. Dean and Clyne [59] showed that, provided the indenter shape is not self-similar, making multiple comparisons on different sections of the same load–displacement plot is similar in effect to the use of multiple indenter shapes. For an indenter with a spherical shape, the stress and strain fields change qualitatively as penetration progresses. Hence, the information being obtained over different depth ranges is analogous to carrying out separate tests with different indenter shapes (reducing the likelihood of different stress–strain curves giving very similar load–displacement plots) [60]. Also, a sphere is much less prone to becoming damaged than other shapes having edges or sharp apex since the sharp tips will wear faster, leading to changes in the tip geometry and resulting tip area function. Spherical-shaped indenters are also easier to specify and manufacture. Finally, using a spherical indenter reduces the risk of encountering computational problems that arise when simulating regions of high local curvature (edges or corners) [60].

Objective function. It is well established that different materials can lead to the same indentation curves [61–64]. Uniqueness of the mechanical properties extracted only from loading/unloading curves is therefore not possible to achieve. For that reason, Bolzon et al. [65] were the first to propose to include the residual imprint after indentation in addition to the load–displacement curve. There exists, however, some arbitrariness when using both, the load–displacement curve and the imprint for the optimization. In that case the objective function would read:

$$\lambda = w_1 \cdot \lambda_{\text{topo}} + w_2 \cdot \lambda_{\text{load–displacement}} \tag{10}$$

However, the selection of an appropriate weight for each part of the objective function is rather arbitrary. Therefore, for the method presented here, only the imprint was used with the additional constraints based on the results from micropillar compression.

6.2. From nano to macro material behavior

Despite many years of experience, it is still a challenge to correlate results of nanoindentation experiments to bulk material behavior. The triaxial mechanical stress state during indentation is different from the one encountered in a uniaxial test. Moreover, nano-mechanical testing involves only a small volume. This can cause a scatter in the results when the microstructure is heterogeneous, depending on whether pre-existing dislocations are present in the test volume or not [56]. Another common feature to all indentation processes is the so called gradient effect, which consists in the development of sharp strain gradients near the indenter tip [66]. These two mechanisms can be seen as part of the more general indentation size effect that describes the increase in hardness with decreasing size of the indent.

The use of a simple phenomenological CP model is therefore only possible if indentation size effects are not significant. From the results in Fig. 16, it becomes clear that the correct load–displacement curve was not captured. The CP model used predicts a much too soft material behavior on the nano scale. When fitting the parameters to this nano scale behavior (not shown), the bulk material is predicted more than twice as hard as in reality. This effect is too big to be explained by friction, tilt, misalignment, and/or other sources of error. The CP model used could clearly not describe the load–displacement curve in nano indentation. Still, the fitting of the pile-up area of the nano indent (along with the additional constraints of the method) can be used successfully to obtain a reasonable mechanical behavior on the macro scale.

6.3. Use of the method in multi-phase materials

The application of this method is a promising path for determining CP parameters for multi-phase materials [67]. For this case, the fit from a macroscopic stress–strain curve only is not possible, since calculating a correct and unique set of CP parameters for each individual phase is not possible. Regarding the creation of the RVE, the distinction between different phases becomes fundamental in order to correctly model the microstructure of the material [68,69].

7. Summary and outlook

An inverse method for determining CP parameters that are representing the bulk behavior of a single BCC phase material has been presented. Its primary experimental input is obtained from nanoindentation. The post-mortem imprint is measured by AFM and compared to a simulated one. The simulations are done using the commercial FEM package MSC.Marc and the CP toolkit DAMASK. The objective function is minimized by a differential evolution algorithm to determine the best fitting CP parameters. As a novelty it is proposed here to simplify the optimization procedure using constraints derived from experiments. The CRSS of the 3 different slip plane families in BCC materials is derived from micropillar compression tests. A direct use of the CRSS values is not possible due to size effects, but they define an upper bound and their ratio is imposed as an additional constraint. The validation of the results in the macroscopic regime is done by comparing a simulated tensile test with an experimental one. The results from two different indents are shown to be reasonably accurate. For getting even better results, the authors propose to combine several indents when evaluating the objective function. Moreover the different indents should be from different orientations. The reason is, that, given a certain orientation, one slip plane family can dominate the deformation, i.e. contribute most shear. If this is the case, the parameters corresponding to the others slip plane families cannot be uniquely determined. However, as a fixed CRSS ratio is used in this work, the effect is less pronounced here.

A differential evolution algorithm is used for the optimization. This allows the search of a global minimum, and therefore, there is no need to provide an initial guess close to the solution. For that case, the often used Nelder–Mead method would have been less suited as it frequently gets stuck in local minima. A potential improvement is proposed by first using the differential evolution algorithm to globally search for a solution, which can then be used as the starting point for the Nelder–Mead algorithm to reach an even better solution.

The importance of a mesh sensitivity analysis for this type of inverse analysis is also demonstrated. Four element types are tested: linear and quadratic hexahedra, each one with reduced- and full-integration schemes. Among these, quadratic elements with reduced integration show the best balance between accuracy, time efficiency, and convergence. As expected, meshes using less distorted elements show better convergence behavior.

The CP parameters identified from optimization without imposing the constraints obtained from the micropillar compression experiment predict a macroscopic material response that is harder than experimentally observed. Therefore, the constraints from micropillar experiments are not just an optional input to reduce the number of independent variables, but are essential for determining suitable CP parameters.

The importance of using a suitable interpolation strategy to compare experimental and simulated data is also demonstrated. Using a Gaussian interpolation approach is shown to give good results when the radius parameter is within a given range. It fails for small radii — which is expected from the fact that the AFM image is not artifact-free — and for large radii — since the interpolation results suffer from the averaging over large areas.

The effect of friction and tilt is discussed. It is shown that a correct modeling of the friction is needed in order to accurately determine the CP parameters. A force-based Coulomb friction model with $\mu = 0.18$ is assumed for this study. The tilt of the experimental surface does not have a big impact on the results when taking it into consideration for the simulation modeling.

This method is a promising path for determining CP parameters in cases where a direct fitting from a macroscopic stress–strain curve is not possible. Even though a unique parameter set was not achieved using a single indent, the macro behavior was reproduced well when using a suitable interpolation method. When combining multiple indents in one objective function as suggested above, there is an expectation of getting at least close to an usable parameter set. In the case of multi-phase materials, this approach allows to determine sets of CP parameters for the individual phases as needed for full field CP simulations.

Funding

This research is part of a collaboration between the Max–Planck-Institut für Eisenforschung and AG der Dillinger Hüttenwerke. C.K. acknowledges funding from the German Research Association (DFG) within the CRC/Transregio TRR188 - project B03.

CRediT authorship contribution statement

Francisco-José Gallardo-Basile: Conceptualization, Software development, Simulations, Data analysis, Experiments, Writing – original draft. **Franz Roters:** Conceptualization, Writing – original draft, Supervision. **Robin M. Jentner:** Experiments. **James P. Best:** Experiments, Supervision. **Christoph Kirchlechner:** Experiments, Supervision. **Kinshuk Srivastava:** Experiments, Supervision. **Sebastian Scholl:** Experiments, Supervision. **Martin Diehl:** Conceptualization, Software development, Writing – original draft, Supervision.

Declaration of competing interest

The authors declare that they have no known competing financial interests or personal relationships that could have appeared to influence the work reported in this paper.

Acknowledgments

F.-J.G.-B. would like to acknowledge the fruitful discussions with Gerhard Dehm. F.-J.G.-B. would like to acknowledge the contribution of Petra Ebbinghaus on the AFM measurements. F.-J.G.-B. would like to acknowledge the contribution of Heidi Bögershausen on the nanoindentation measurements.

All authors have read and agreed to the published version of the manuscript.

References

[1] F. Roters, P. Eisenlohr, L. Hantcherli, D.D. Tjahjanto, T.R. Bieler, D. Raabe, Overview of constitutive laws, kinematics, homogenization, and multiscale methods in crystal plasticity finite element modeling: Theory, experiments, applications, Acta Mater. (2010) http://dx.doi.org/10.1016/j.actamat.2009.10.058.

[2] F. Roters, P. Eisenlohr, T.R. Bieler, D. Raabe, Crystal Plasticity Finite Element Methods in Materials Science and Engineering, Wiley-VCH, 2010, http://dx.doi.org/10.1002/9783527631483.

[3] C. Miehe, J. Schröder, J. Schotte, Computational homogenization analysis in finite plasticity Simulation of texture development in polycrystalline materials, Comput. Methods Appl. Mech. Engrg. (1999) http://dx.doi.org/10.1016/S0045-7825(98)00218-7.

[4] H. Wang, B. Raeisinia, P.D. Wu, S.R. Agnew, C.N. Tomé, Evaluation of self-consistent polycrystal plasticity models for magnesium alloy AZ31B sheet, Int. J. Solids Struct. (2010) http://dx.doi.org/10.1016/j.ijsolstr.2010.06.016.

[5] J. Segurado, J. Llorca, Simulation of the deformation of polycrystalline nanostructured Ti by computational homogenization, Comput. Mater. Sci. (2013) http://dx.doi.org/10.1016/j.commatsci.2013.03.008.

[6] V. Herrera-Solaz, J. LLorca, E. Dogan, I. Karaman, J. Segurado, An inverse optimization strategy to determine single crystal mechanical behavior from polycrystal tests: Application to AZ31 Mg alloy, Int. J. Plast. (2014) http://dx.doi.org/10.1016/j.ijplas.2014.02.001.

[7] K. Sedighiani, M. Diehl, K. Traka, F. Roters, J. Sietsma, D. Raabe, An efficient and robust approach to determine material parameters of crystal plasticity constitutive laws from macro-scale stress–strain curves, Int. J. Plast. (2020) http://dx.doi.org/10.1016/j.ijplas.2020.102779.

[8] M. Diehl, J. Niehuesbernd, E. Bruder, Quantifying the contribution of crystallographic texture and grain morphology on the elastic and plastic anisotropy of BCC steel, Metals (2019) http://dx.doi.org/10.3390/met9121252.

[9] M. Diehl, M. Groeber, C. Haase, D.A. Molodov, F. Roters, D. Raabe, Identifying structure–property relationships through DREAM.3D representative volume elements and DAMASK crystal plasticity simulations: An integrated computational materials engineering approach, J. Miner. Met. Mater. Soc. (2017) http://dx.doi.org/10.1007/s11837-017-2303-0.

[10] F.-J. Gallardo-Basile, Y. Naunheim, F. Roters, M. Diehl, Lath martensite microstructure modeling: A high-resolution crystal plasticity simulation study, Materials (2021) http://dx.doi.org/10.3390/ma14030691.

[11] T.B. Britton, F.P.E. Dunne, A.J. Wilkinson, On the mechanistic basis of deformation at the microscale in hexagonal close-packed metals, Proc. R. Soc. A (2015) http://dx.doi.org/10.1098/rspa.2014.0881.

[12] A.H. Cottrell, Dislocations and Plastic Flow in Crystals, Oxford University Press, 1953.

[13] D. Hull, D.J. Bacon, Introduction to Dislocations, fifth ed., Butterworth-Heinemann, 2011.

[14] M. Bertin, C. Du, J.P.M. Hoefnagels, F. Hild, Crystal plasticity parameter identification with 3D measurements and integrated digital image correlation, Acta Mater. (2016) http://dx.doi.org/10.1016/j.actamat.2016.06.039.

[15] C. Du, F. Maresca, M.G.D. Geers, J.P.M. Hoefnagels, Ferrite slip system activation investigated by uniaxial micro-tensile tests and simulations, Acta Mater. (2018) http://dx.doi.org/10.1016/j.actamat.2017.12.054.

[16] H. Ghassemi-Armaki, P. Chen, S. Bhat, S. Sadagopan, S. Kumar, A. Bower, Microscale-calibrated modeling of the deformation response of low-carbon martensite, Acta Mater. (2013) http://dx.doi.org/10.1016/j.actamat.2013.02.051.

[17] G. Dehm, B.N. Jaya, R. Raghavan, C. Kirchlechner, Overview on micro- and nanomechanical testing: New insights in interface plasticity and fracture at small length scales, Acta Mater. (2018) http://dx.doi.org/10.1016/j.actamat.2017.06.019.

[18] J. Lee, C. Lee, B. Kim, Reverse analysis of nano-indentation using different representative strains and residual indentation profiles, Mater. Des. (2009-10) http://dx.doi.org/10.1016/j.matdes.2009.03.030.

[19] P. Haušild, A. Materna, J. Nohava, On the identification of stress–strain relation by instrumented indentation with spherical indenter, Mater. Des. (2012) http://dx.doi.org/10.1016/j.matdes.2012.01.025.

[20] C. Moussa, X. Hernot, O. Bartier, G. Delattre, G. Mauvoisin, Evaluation of the tensile properties of a material through spherical indentation: Definition of an average representative strain and a confidence domain, J. Mater. Sci. (2013) http://dx.doi.org/10.1007/s10853-013-7739-1.

[21] Y. Cao, J. Lu, A new method to extract the plastic properties of metal materials from an instrumented spherical indentation loading curve, Acta Mater. (2004) http://dx.doi.org/10.1016/j.actamat.2004.05.018.

[22] J. Lee, T. Kim, H. Lee, A study on robust indentation techniques to evaluate elastic–plastic properties of metals, Int. J. Solids Struct. (2010) http://dx.doi.org/10.1016/j.ijsolstr.2009.11.003.

[23] M.K. Khan, S.V. Hainsworth, M.E. Fitzpatrick, L. Edwards, A combined experimental and finite element approach for determining mechanical properties of aluminium alloys by nanoindentation, Comput. Mater. Sci. (2010) http://dx.doi.org/10.1016/j.commatsci.2010.06.018.

[24] J.E. Campbell, R.P. Thompson, J. Dean, T.W. Clyne, Experimental and computational issues for automated extraction of plasticity parameters from spherical indentation, Mech. Mater. (2018) http://dx.doi.org/10.1016/j.mechmat.2018.06.004.

[25] Y. Hwang, K. Marimuthu, N. Kim, C. Lee, H. Lee, Extracting plastic properties from in-plane displacement data of spherical indentation imprint, Int. J. Mech. Sci. (2021) http://dx.doi.org/10.1016/j.ijmecsci.2021.106291.

[26] C. Zambaldi, Y. Yang, T.R. Bieler, D. Raabe, Orientation informed nanoindentation of α-titanium: Indentation pileup in hexagonal metals deforming by prismatic slip, J. Mater. Res. (2012) http://dx.doi.org/10.1557/jmr.2011.334.

[27] C.C. Tasan, J.P.M. Hoefnagels, M. Diehl, D. Yan, F. Roters, D. Raabe, Strain localization and damage in dual phase steels investigated by coupled in-situ deformation experiments-crystal plasticity simulations, Int. J. Plast. (2014) http://dx.doi.org/10.1016/j.ijplas.2014.06.004.

[28] A. Chakraborty, P. Eisenlohr, Evaluation of an inverse methodology for estimating constitutive parameters in face-centered cubic materials from single crystal indentations, Eur. J. Mech. A Solids (2017) http://dx.doi.org/10.1016/j.euromechsol.2017.06.012.

[29] M. Shahmardani, N. Vajragupta, A. Hartmaier, Robust optimization scheme for inverse method for crystal plasticity model parametrization, Materials (2020) http://dx.doi.org/10.3390/ma13030735.

[30] J.K. Engels, N. Vajragupta, A. Hartmaier, Parameterization of a non-local crystal plasticity model for tempered lath martensite using nanoindentation and inverse method, Front. Mater. (2019) http://dx.doi.org/10.3389/fmats.2019.00247.

[31] C. Tian, D. Ponge, L. Christiansen, C. Kirchlechner, On the mechanical heterogeneity in dual phase steel grades: Activation of slip systems and deformation of martensite in DP800, Acta Mater. (2020) http://dx.doi.org/10.1016/j.actamat.2019.11.002.

[32] M.S. Duesbery, V. Vitek, Plastic anisotropy in B.C.C. transition metals, Acta Mater. (1998) http://dx.doi.org/10.1016/S1359-6454(97)00367-4.

[33] L. Dezerald, D. Rodney, E. Clouet, L. Ventelon, F. Willaime, Plastic anisotropy and dislocation trajectory in BCC metals, Nature Commun. (2016) http://dx.doi.org/10.1038/ncomms11695.

[34] W.C. Oliver, G.M. Pharr, An improved technique for determining hardness and elastic modulus using load and displacement sensing indentation experiments, J. Mater. Res. (1992) http://dx.doi.org/10.1557/JMR.1992.1564.

[35] D. Nečas, P. Klapetek, Gwyddion: An open-source software for SPM data analysis, Central Eur. J. Phys. (2012) http://dx.doi.org/10.2478/s11534-011-0096-2.

[36] F. Roters, M. Diehl, P. Shanthraj, P. Eisenlohr, C. Reuber, S.L. Wong, T. Maiti, A. Ebrahimi, T. Hochrainer, H.-O. Fabritius, S. Nikolov, M. Friak, N. Fujita, N. Grilli, K.G.F. Janssens, N. Jia, P.J.J. Kok, D. Ma, F. Meier, E. Werner, M. Stricker, D. Weygand, D. Raabe, DAMASK – the Düsseldorf advanced material simulation kit for modelling multi-physics crystal plasticity, damage, and thermal phenomena from the single crystal up to the component scale, Comput. Mater. Sci. (2019) http://dx.doi.org/10.1016/j.commatsci.2018.04.030.

[37] J.W. Hutchinson, Bounds and self-consistent estimates for creep of polycrystalline materials, Proc. R. Soc. Lond. Ser. A (1976) http://dx.doi.org/10.1098/rspa.1976.0027.

[38] D. Mercier, C. Zambaldi, T.R. Bieler, A Matlab toolbox to analyze slip transfer through grain boundaries, in: Proc. 17th Int. Conf. Textures of Materials, ICOTOM-17, 2015, http://dx.doi.org/10.1088/1757-899X/82/1/012090.

[39] Marc® 2021.4 Volume A: Theory and User Information, 2021.

[40] P. Eisenlohr, M. Diehl, R.A. Lebensohn, F. Roters, A spectral method solution to crystal elasto-viscoplasticity at finite strains, Int. J. Plast. (2013) http://dx.doi.org/10.1016/j.ijplas.2012.09.012.

[41] P. Shanthraj, P. Eisenlohr, M. Diehl, F. Roters, Numerically robust spectral methods for crystal plasticity simulations of heterogeneous materials, Int. J. Plast. (2015) http://dx.doi.org/10.1016/j.ijplas.2014.02.006.

[42] M.A. Groeber, M.A. Jackson, DREAM.3D: A digital representation environment for the analysis of microstructure in 3D, Integr. Mater. Manuf. Innov. (2014) http://dx.doi.org/10.1186/2193-9772-3-5.

[43] F. Bachmann, R. Hielscher, H. Schaeben, Texture analysis with MTEX – free and open source software toolbox, Solid State Phenomena (2010) http://dx.doi.org/10.4028/www.scientific.net/SSP.160.63.

[44] P. Eisenlohr, F. Roters, Selecting sets of discrete orientations for accurate texture reconstruction, Comput. Mater. Sci. (2008) http://dx.doi.org/10.1016/j.commatsci.2007.09.015.

[45] R. Madec, L.P. Kubin, Dislocation strengthening in FCC metals and in BCC metals at high temperatures, Acta Mater. (2017) http://dx.doi.org/10.1016/j.actamat.2016.12.040.

[46] U.F. Kocks, The relation between polycrystal deformation and single-crystal deformation, Metall. Mater. Trans. B 1 (5) (1970) 1121–1143, http://dx.doi.org/10.1007/bf02900224.

[47] J.A. Nelder, R. Mead, A Simplex Method for Function Minimization, Comput. J. (1965) http://dx.doi.org/10.1093/comjnl/7.4.308.

[48] R. Storn, K. Price, Differential evolution – A simple and efficient heuristic for global optimization over continuous spaces, J. Global Optim. (1997) http://dx.doi.org/10.1023/a:1008202821328.

[49] B. Tang, Orthogonal array-based latin hypercubes, J. Amer. Statist. Assoc. (1993) http://dx.doi.org/10.1080/01621459.1993.10476423.

[50] P. Virtanen, R. Gommers, T.E. Oliphant, M. Haberland, T. Reddy, D. Cournapeau, E. Burovski, P. Peterson, W. Weckesser, J. Bright, S.J. van der Walt, M. Brett, J. Wilson, K.J. Millman, N. Mayorov, A.R.J. Nelson, E. Jones, R. Kern, E. Larson, C.J. Carey, I. Polat, Y. Feng, E.W. Moore, J. VanderPlas, D. Laxalde, J. Perktold, R. Cimrman, I. Henriksen, E.A. Quintero, C.R. Harris, A.M. Archibald, A.H. Ribeiro, F. Pedregosa, P. van Mulbregt, A. Vijaykumar, A.P. Bardelli, A. Rothberg, A. Hilboll, A. Kloeckner, A. Scopatz, A. Lee, A. Rokem, C.N. Woods, C. Fulton, C. Masson, C. Häggström, C. Fitzgerald, D.A. Nicholson, D.R. Hagen, D.V. Pasechnik, E. Olivetti, E. Martin, E. Wieser, F. Silva, F. Lenders, F. Wilhelm, G. Young, G.A. Price, G.-L. Ingold, G.E. Allen, G.R. Lee, H. Audren, I. Probst, J.P. Dietrich, J. Silterra, J.T. Webber, J. Slavič, J. Nothman, J. Buchner, J. Kulick, J.L. Schönberger, J.V. de Miranda Cardoso, J. Reimer, J. Harrington, J.L.C. Rodriguez, J. Nunez-Iglesias, J. Kuczynski, K. Tritz, M. Thoma, M. Newville, M. Kümmerer, M. Bolingbroke, M. Tartre, M. Pak, N.J. Smith, N. Nowaczyk, N. Shebanov, O. Pavlyk, P.A. Brodtkorb, P. Lee, R.T. McGibbon, R. Feldbauer, S. Lewis, S. Tygier, S. Sievert, S. Vigna, S. Peterson, S. More, T. Pudlik, T. Oshima, T.J. Pingel, T.P. Robitaille, T. Spura, T.R. Jones, T. Cera, T. Leslie, T. Zito, T. Krauss, U. Upadhyay, Y.O. Halchenko, Y. Vázquez-Baeza, SciPy 1.0: Fundamental algorithms for scientific computing in Python, Nature Methods (2020) http://dx.doi.org/10.1038/s41592-019-0686-2.

[51] U. Ayachit, the ParaView Guide : Upyeard for ParaView Version 4.3, Kitware, 2015.
[52] C. Hansen, The Visualization Handbook, Elsevier Butterworth-Heinemann, 2005.
[53] C. Sullivan, A. Kaszynski, PyVista: 3D plotting and mesh analysis through a streamlined interface for the Visualization Toolkit (VTK), J. Open Source Softw. (2019) http://dx.doi.org/10.21105/joss.01450.
[54] J.J. Kang, A.A. Becker, W. Sun, Determining elastic–plastic properties from indentation data obtained from finite element simulations and experimental results, Int. J. Mech. Sci. (2012) http://dx.doi.org/10.1016/j.ijmecsci.2012.05.011.
[55] H. Hyun, M. Kim, J. Lee, H. Lee, A dual conical indentation technique based on FEA solutions for property evaluation, Mech. Mater. (2011) http://dx.doi.org/10.1016/j.mechmat.2011.03.003.
[56] P.S. Engels, C. Begau, S. Gupta, B. Schmaling, A. Ma, A. Hartmaier, Multiscale Modeling of Nanoindentation: From Atomistic to Continuum Models, Springer, Netherlands, 2014, pp. 285–322, http://dx.doi.org/10.1007/978-94-007-6919-_15.
[57] J.L. Bucaille, S. Stauss, E. Felder, J. Michler, Determination of plastic properties of metals by instrumented indentation using different sharp indenters, Acta Mater. (2003) http://dx.doi.org/10.1016/s1359-6454(02)00568-2.
[58] C. Heinrich, A.M. Waas, A.S. Wineman, Determination of material properties using nanoindentation and multiple indenter tips, Int. J. Solids Struct. (2009-01) http://dx.doi.org/10.1016/j.ijsolstr.2008.08.042.
[59] J. Dean, T.W. Clyne, Extraction of plasticity parameters from a single test using a spherical indenter and FEM modelling, Mech. Mater. (2017) http://dx.doi.org/10.1016/j.mechmat.2016.11.014.
[60] T.W. Clyne, J.E. Campbell, M. Burley, J. Dean, Profilometry-based inverse finite element method indentation plastometry, Adv. Eng. Mater. (2021) http://dx.doi.org/10.1002/adem.202100437.
[61] J. Alkorta, J.M. Martínez-Esnaola, J.G. Sevillano, Absence of one-to-one correspondence between elastoplastic properties and sharp-indentation load–penetration data, J. Mater. Res. (2005) http://dx.doi.org/10.1557/jmr.2005.0053.
[62] Y.-T. Cheng, C.-M. Cheng, Can stress–strain relationships be obtained from indentation curves using conical and pyramidal indenters? J. Mater. Res. (1999) http://dx.doi.org/10.1557/jmr.1999.0472.
[63] T.W. Capehart, Y.-T. Cheng, Determining constitutive models from conical indentation: Sensitivity analysis, J. Mater. Res. (2003) http://dx.doi.org/10.1557/jmr.2003.0113.
[64] K.K. Tho, S. Swaddiwudhipong, Z.S. Liu, K. Zeng, J. Hua, Uniqueness of reverse analysis from conical indentation tests, J. Mater. Res. (2004) http://dx.doi.org/10.1557/jmr.2004.0306.
[65] G. Bolzon, G. Maier, M. Panico, Material model calibration by indentation, imprint mapping and inverse analysis, Int. J. Solids Struct. (2004) http://dx.doi.org/10.1016/j.ijsolstr.2004.01.025.
[66] G. Mokios, E.C. Aifantis, Gradient effects in micro-/nanoindentation, Mater. Sci. Technol. (2012) http://dx.doi.org/10.1179/1743284712y.0000000053.
[67] F.-J. Gallardo-Basile, F. Roters, R.M. Jentner, K. Srivastava, S. Scholl, M. Diehl, Modeling bainite dual-phase steels: A high-resolution crystal plasticity simulation study, Crystals (2023) http://dx.doi.org/10.3390/cryst13040673.
[68] K. Zhu, D. Barbier, T. Iung, Characterization and quantification methods of complex BCC matrix microstructures in advanced high strength steels, J. Mater. Sci. (2012-08) http://dx.doi.org/10.1007/s10853-012-6756-9.
[69] R.M. Jentner, K. Srivastava, S. Scholl, F.-J. Gallardo-Basile, J.P. Best, C. Kirchlechner, G. Dehm, Unsupervised clustering of nanoindentation data for microstructural reconstruction: Challenges in phase discrimination, Materialia (2023) 101750, http://dx.doi.org/10.1016/j.mtla.2023.101750.